

July 18th, 2015

Editor for *Geoscientific Model Development*

Dear Editor Dr. Williams,

Thank you for the support of this study. We are re-submitting the manuscript entitled “The Yale Interactive terrestrial Biosphere Model version 1.0: description, evaluation and implementation into NASA GISS ModelE2” to *Geoscientific Model Development*.

All three points you suggested have been implemented into this version of paper to reflect proper citations and acknowledgements. These changes include:

“For the YIBs model, we build on the phenology scheme of Kim et al. (2015) and extend it based on long-term measurements of leaf phenology at 5 U.S. sites ...” (section 3.2)

“Similar to the approach outlined in Kim et al. (2015), the onset of greenness is triggered if the GDD exceeds a threshold value ...” (section 3.2.1)

“Similar to DBF, the onset of grass greenness is triggered if *SGDD* is higher than a threshold value *SG_b* (Kim et al., 2015)” (section 3.2.3)

“We are grateful to Y. Kim, I. Aleinov, and N. Y. Kiang for access to unpublished codes.” (Acknowledgements)

A new reference is added as:

Kim, Y., Moorcroft, P. R., Aleinov, I., Puma, M. J., and Kiang, N. Y.: Variability of phenology and fluxes of water and carbon with observed and simulated soil moisture in the Ent Terrestrial Biosphere Model (Ent TBM version 1.0.1.0.0), *Geosci. Model Dev. Discuss.*, in press, 2015.

A mark-up version of manuscript is attached with this response at the end.

Thanks for your consideration of our submission.

Sincerely,

Xu Yue
School of Forestry and Environmental Studies
Yale University
New Haven, CT, 06511, USA
E-mail: xuyueseas@gmail.com

1 **The Yale Interactive terrestrial Biosphere Model version 1.0: description,**
2 **evaluation and implementation into NASA GISS ModelE2**

3

4 X. Yue and N. Unger

5

6 School of Forestry and Environment Studies, Yale University, New Haven, Connecticut
7 06511, USA

8

9

Abstract

The land biosphere, atmospheric chemistry and climate are intricately interconnected yet the modeling of carbon-climate and chemistry-climate interactions have evolved as entirely separate research communities. We describe the **Yale Interactive terrestrial Biosphere (YIBs)** model version 1.0, a land carbon cycle model that has been developed for coupling to the NASA Goddard Institute for Space Studies (GISS) ModelE2 global chemistry-climate model. The YIBs model adapts routines from the mature TRIFFID and CASA models to simulate interactive carbon assimilation, allocation, and autotrophic and heterotrophic respiration. Dynamic daily leaf area index is simulated based on carbon allocation and temperature- and drought-dependent prognostic phenology. YIBs incorporates a semi-mechanistic ozone vegetation damage scheme. Here, we validate the present day YIBs land carbon fluxes for three increasingly complex configurations: (i) off-line local site-level (ii) off-line global forced with WFDEI (WATCH Forcing Data methodology applied to ERA-Interim data) meteorology (iii) on-line coupled to the NASA ModelE2 (NASA ModelE2-YIBs). Off-line YIBs has hourly and on-line YIBs has half-hourly temporal resolution. The large observational database used for validation includes carbon fluxes from 145 flux tower sites and multiple satellite products. At the site level, YIBs simulates reasonable seasonality (correlation coefficient $R > 0.8$) of gross primary productivity (GPP) at 121 out of 145 sites with biases in magnitude ranging from -19% to 7% depending on plant functional type. On the global scale, the off-line model simulates an annual GPP of 125 ± 3 petagrams of carbon (Pg C) and net ecosystem exchange (NEE) of -2.5 ± 0.7 Pg C for 1982-2011, with seasonality and spatial distribution consistent with the satellite observations. We assess present day global ozone vegetation damage using the off-line YIBs configuration. Ozone damage reduces global GPP by 2-5% annually with regional extremes of 4-10% in East Asia. The on-line model simulates annual GPP of 123 ± 1 Pg C and NEE of -2.7 ± 0.7 Pg C. NASA ModelE2-YIBs is a useful new tool to investigate coupled interactions between the land carbon cycle, atmospheric chemistry, and climate change.

Keywords: terrestrial biosphere model, carbon cycle, photosynthesis, ozone, phenology, gross primary productivity, net ecosystem exchange

1. Introduction

The terrestrial biosphere interacts with the atmosphere through the exchanges of energy, carbon, reactive gases, water, and momentum fluxes. Forest ecosystems absorb an estimated 120 petagrams of carbon (Pg C) per year from the atmosphere (Beer et al., 2010) and mitigate about one quarter of the anthropogenic carbon dioxide (CO₂) emissions (Friedlingstein et al., 2014). This carbon assimilation is sensitive to human-caused perturbations including climate change and land use change (Zhao and Running, 2010; Houghton et al., 2012), and is affected by atmospheric pollutants such as ozone and aerosols (Sitch et al., 2007; Mercado et al., 2009). Over the past 2-3 decades, a number of terrestrial biosphere models have been developed as tools to quantify the present-day global carbon budget in conjunction with available but sparse observations (e.g., Jung et al., 2009), to understand the relationships between terrestrial biospheric fluxes and environmental conditions (e.g., Zeng et al., 2005), to attribute drivers of trends in the carbon cycle during the anthropogenic era (e.g., Sitch et al., 2015), and to project future changes in the land biosphere and the consequences for regional and global climate change (e.g., Friedlingstein et al., 2006).

Emerging research identifies climatically-relevant interactions between the land biosphere and atmospheric chemistry (e.g., Huntingford et al., 2011). For instance, stomatal uptake is an important sink of tropospheric ozone (Val Martin et al., 2014), but damages photosynthesis, reduces plant growth and biomass accumulation, limits crop yields, and affects stomatal control over plant transpiration of water vapor between the leaf surface and atmosphere (Ainsworth et al., 2012; Hollaway et al., 2012). The indirect CO₂ radiative forcing due to the vegetation damage effects of anthropogenic ozone increases since the industrial revolution may be as large as +0.4 W m⁻² (Sitch et al., 2007), which is 25% of the magnitude of the direct CO₂ radiative forcing over the same period, and of similar magnitude to the direct ozone radiative forcing. Atmospheric oxidation of biogenic volatile organic compound (BVOC) emissions affects surface air quality and exerts additional regional and global chemical climate forcings (Scott et al., 2014; Unger, 2014a, b). Fine mode atmospheric pollution particles affect the land biosphere by changing the physical climate state and through diffuse radiation

fertilization (Mercado et al., 2009; Mahowald, 2011). Land plant phenology has experienced substantial changes in the last few decades (Keenan et al., 2014), possibly influencing both ozone deposition and BVOC emissions through the extension of growing seasons. These coupled interactions are often not adequately represented in current generation land biosphere models or global chemistry-climate models. Global land carbon cycle models often prescribe off-line ozone and aerosol fields (e.g., Sitch et al., 2007; Mercado et al., 2009), and global chemistry-climate models often prescribe fixed off-line vegetation fields (e.g., Lamarque et al., 2013; Shindell et al., 2013a). However, multiple mutual feedbacks occur between vegetation physiology and reactive atmospheric chemical composition that are completely neglected using these previous off-line approaches. Model frameworks are needed that fully 2-way couple the land carbon cycle and atmospheric chemistry, and simulate the consequences for climate change.

Our objective is to present the description and present-day evaluation of the Yale Interactive terrestrial Biosphere (YIBs) model version 1.0 that has been developed for the investigation of carbon-chemistry-climate interactions. The YIBs model can be used in three configurations: (i) off-line local site-level (ii) off-line global forced with WFDEI (WATCH Forcing Data methodology applied to ERA-Interim data) meteorology (iii) on-line coupled to the latest frozen version of the NASA GISS ModelE2 (Schmidt et al., 2014). The global climate model represents atmospheric gas-phase and aerosol chemistry, cloud, radiation, and land surface processes, and has been widely used for studies of atmospheric components, climate change, and their interactions (Schmidt et al., 2006; Koch et al., 2011; Unger, 2011; Shindell et al., 2013b; Miller et al., 2014). To our knowledge, this study represents the first description and validation of an interactive climate-sensitive closed land carbon cycle in NASA ModelE2. The impacts of the updated vegetation scheme on the chemistry and climate simulations in NASA ModelE2 will be addressed in other on-going research. Section 2 describes the observational datasets used to evaluate YIBs land carbon cycle performance. Section 3 describes physical parameterizations of the vegetation model. Section 4 explains the model set up

and simulations in three configurations. Section 5 presents the results of the model evaluation and section 6 summarizes the model performance.

1.1 YIBs design strategy

Many land carbon cycle models already exist (e.g. Sitch et al., 2015 and references therein; Schaefer et al., 2012 and references therein). We elected to build YIBs in a step-by-step process such that our research group has intimate familiarity with the underlying scientific processes, rather than adopting an existing model as a “black box”. This unconventional interdisciplinary approach is important for discerning the complex mutual feedbacks between atmospheric chemistry and the land carbon sink under global change. The development of YIBs land carbon cycle model has proceeded in three main steps. The first step was the implementation of vegetation biophysics, photosynthesis-dependent BVOC emissions and ozone vegetation damage that have been extensively documented, validated and applied in 7 previous publications (Unger, 2013; Unger et al., 2013; Unger, 2014a, b; Unger and Yue, 2014; Yue and Unger, 2014; Zheng et al., 2015). The second step was the selection of the YIBs default phenology scheme based on rigorous inter-comparison of 13 published phenological models (Yue et al., 2015a). This study represents the third step to simulate the closed climate-sensitive land carbon cycle: implementation of interactive carbon assimilation, allocation, autotrophic and heterotrophic respiration, and dynamic tree growth (changes in both height and LAI). For this third step, we purposefully select the mature, well-supported, well-established, readily available and accessible community algorithms: TRIFFID (Cox, 2001; Clark et al., 2011) and the Carnegie-Ames-Stanford Approach (CASA) (Potter et al., 1993; Schaefer et al., 2008). TRIFFID has demonstrated previous usage in carbon-chemistry-climate interactions research.

2. Observational datasets for validation

2.1 Site-level measurements

To validate the YIBs model, we use eddy covariance measurements from 145 flux tower sites (Fig. 1), which are collected by the North American Carbon Program (Schaefer et al., 2012) (K. Schaefer, personal communication) and downloaded from the FLUXNET (<http://fluxnet.ornl.gov>) network. Among these sites, 138 are located in the Northern Hemisphere, with 74 in Europe, 38 in U.S., and 24 in Canada (Table S1). Sites on other continents are limited. Most of the sites have one dominant plant functional type (PFT), including 54 sites of evergreen needleleaf forests (ENF), 20 deciduous broadleaf forests (DBF), 9 evergreen broadleaf forests (EBF), 28 grasslands, 18 shrublands, and 16 croplands. We attribute sites with mixed forest to the ENF as these sites are usually at high latitudes. Each site dataset provides hourly or half-hourly measurements of carbon fluxes, including gross primary productivity (GPP) and net ecosystem exchange (NEE), and CO₂ concentrations and meteorological variables, such as surface air temperature, relative humidity, wind speed, and shortwave radiation.

2.2 Global measurements

We use global tree height, leaf area index (LAI), GPP, net primary productivity (NPP), and phenology datasets to validate the vegetation model. Canopy height is retrieved using 2005 remote sensing data from the Geoscience Laser Altimeter System (GLAS) aboard ICESat satellite (Simard et al., 2011). LAI measurements for 1982-2011 are derived using the Normalized Difference Vegetation Index (NDVI) from Global Inventory Modeling and Mapping Studies (GIMMS) (Zhu et al., 2013). Global GPP observations of 1982-2011 are estimated based on the upscaling of FLUXNET eddy covariance data with a biosphere model (Jung et al., 2009). This product was made to reproduce a model (LPJmL) using the fraction of absorbed PAR simulated in LPJmL. As a comparison, we also use GPP observations of 1982-2008 derived based on FLUXNET, satellite, and meteorological observations (Jung et al., 2011), which is about 10% lower than that of Jung et al. (2009). The NPP for 2000-2011 is derived using remote sensing data from Moderate Resolution Imaging Spectroradiometer (MODIS) (Zhao et al., 2005). We use the global retrieval of greenness onset derived from the Advanced Very High Resolution

Radiometer (AVHRR) and the MODIS data from 1982 to 2011 (Zhang et al., 2014). All datasets are interpolated to the $1^\circ \times 1^\circ$ off-line model resolution for comparisons.

3. YIBs model description

3.1 Vegetation biophysics

YIBs calculates carbon uptake for 9 PFTs: tundra, C3/C4 grass, shrubland, DBF, ENF, EBF, and C3/C4 cropland (Table 1). In the gridded large-scale model applications, each model PFT fraction in the vegetated part of each grid cell represents a single canopy. The vegetation biophysics simulates C3 and C4 photosynthesis with the well-established Michealis-Menten enzyme-kinetics scheme (Farquhar et al., 1980; von Caemmerer and Farquhar, 1981) and the stomatal conductance model of Ball and Berry (Ball et al., 1987). The total leaf photosynthesis (A_{tot} , $\mu\text{mol m}^{-2} [\text{leaf}] \text{ s}^{-1}$) is limited by one of three processes: (i) the capacity of the ribulose 1,5-bisphosphate (RuBP) carboxylase-oxygenase enzyme (Rubisco) to catalyze carbon fixation (J_c); (ii) the capacity of the Calvin cycle and the thylakoid reactions to regenerate RuBP supported by electron transport (J_e); (iii) the capacity of starch and sucrose synthesis to regenerate inorganic phosphate for photo-phosphorylation in C3 plants and phosphoenolpyruvate (PEP) in C4 plants (J_s).

$$A_{tot} = \min(J_c, J_e, J_s) \quad (1)$$

The J_c , J_e , and J_s are parameterized as functions of environmental variables (e.g. temperature, radiation, and CO_2 concentrations) and the maximum carboxylation capacity (V_{cmax} , $\mu\text{mol m}^{-2} \text{ s}^{-1}$) (Collatz et al., 1991; Collatz et al., 1992):

$$J_c = \begin{cases} V_{cmax} \left(\frac{c_i - \Gamma_*}{c_i + K_c (1 + O_i / K_o)} \right) & \text{for C3 plant} \\ V_{cmax} & \text{for C4 plant} \end{cases} \quad (2)$$

$$J_e = \begin{cases} a_{leaf} \cdot PAR \cdot \alpha \cdot \left(\frac{c_i - \Gamma^*}{c_i + 2\Gamma^*} \right) & \text{for C3 plant} \\ a_{leaf} \cdot PAR \cdot \alpha & \text{for C4 plant} \end{cases} \quad (3)$$

$$J_s = \begin{cases} 0.5V_{cmax} & \text{for C3 plant} \\ K_s \cdot V_{cmax} \cdot \frac{c_i}{P_s} & \text{for C4 plant} \end{cases} \quad (4)$$

where c_i and O_i are the leaf internal partial pressure (Pa) of CO_2 and oxygen, Γ^* (Pa) is the CO_2 compensation point, K_c and K_o (Pa) are Michaelis-Menten parameters for the carboxylation and oxygenation of rubisco. The parameters K_c , K_o , and Γ^* vary with temperature according to a Q_{10} function. PAR ($\mu\text{mol m}^{-2} \text{s}^{-1}$) is the incident photosynthetically active radiation, a_{leaf} is leaf-specific light absorbance, and α is intrinsic quantum efficiency. P_s is the ambient pressure and K_s is a constant set to 4000 following Oleson et al. (2010). V_{cmax} is a function of the optimal V_{cmax} at 25 °C (V_{cmax25}) based on a Q_{10} function.

Net carbon assimilation (A_{net}) of leaf is given by:

$$A_{net} = A_{tot} - R_d \quad (5)$$

where R_d is the rate of dark respiration set to 0.011 V_{cmax} for C3 plants (Farquhar et al., 1980) and 0.025 V_{cmax} for C4 plants (Clark et al., 2011). The stomatal conductance of water vapor (g_s in $\text{mol [H}_2\text{O]} \text{ m}^{-2} \text{s}^{-1}$) is dependent on net photosynthesis:

$$g_s = m \frac{A_{net} \cdot RH}{c_s} + b \quad (6)$$

where m and b are the slope and intercept derived from empirical fitting to the Ball and Berry stomatal conductance equations, RH is relative humidity, and c_s is the CO_2 concentration at the leaf surface. In the model, the slope m is influenced by water stress,

so that drought decreases photosynthesis by affecting stomatal conductance. Appropriate photosynthesis parameters for different PFTs are taken from Friend and Kiang (2005) and the Community Land Model (Oleson et al., 2010) with updates from Bonan et al. (2011) (Table 1). In future work, we will investigate the carbon-chemistry-climate impacts of updated stomatal conductance models in YIBs (Berry et al., 2010; Pieruschka et al., 2010; Medlyn et al., 2011).

The coupled equation system of photosynthesis, stomatal conductance and CO₂ diffusive flux transport equations form a cubic in A_{net} that is solved analytically (Baldocchi, 1994). A simplified but realistic representation of soil water stress β is included in the vegetation biophysics following the approach of Porporato et al. (2001). The algorithm reflects the relationship between soil water amount and the extent of stomatal closure ranging from no water stress to the soil moisture stress onset point (s^*) through to the wilting point (s_{wilt}). Stomatal conductance is reduced linearly between the PFT-specific values of s^* and s_{wilt} based on the climate model's soil water volumetric saturation in 6 soil layers (Unger et al., 2013).

The canopy radiative transfer scheme divides the canopy into an adaptive number of layers (typically 2-16) for light stratification. Each canopy layer distinguishes sunlit and shaded portions of leaves, so that the direct and diffuse photosynthetically active radiation (PAR) is used for carbon assimilation respectively (Spitters et al., 1986). The leaf photosynthesis is then integrated over all canopy layers to generate the GPP:

$$GPP = \int_0^{LAI} A_{tot} dL \quad (7)$$

3.2 Leaf phenology

Phenology determines the annual cycle of LAI. Plant phenology is generally controlled by temperature, water availability, and photoperiod (Richardson et al., 2013). For deciduous trees, the timing of budburst is sensitive to temperature (Vitasse et al., 2009) and the autumn senescence is related to both temperature and photoperiod (Delpierre et al., 2009). For small trees and grasses, such as tundra, savanna, and shrubland, phenology

is controlled by temperature and/or soil moisture, depending on the species type and locations of the vegetation (Delbart and Picard, 2007; Liu et al., 2013). In the YIBs model, leaf phenology is updated on a daily basis. For the YIBs model, [we build on the phenology scheme of Kim et al. \(2015\) and extend it based on](#) long-term measurements of leaf phenology at 5 U.S. sites (Yue et al., 2015a, hereinafter Y2015) and GPP at the 145 flux tower sites. A summary of the phenological parameters adopted is listed in Table 2.

3.2.1 Deciduous broadleaf forest (DBF)

We predict spring phenology of DBF using the cumulative thermal summation (White et al., 1997). The accumulative growing degree day (GDD) is calculated for the n th day from winter solstice if the 10-day average air temperature T_{10} is higher than a base temperature T_b :

$$GDD = \sum_{i=1}^n \max(T_{10} - T_b, 0) \quad (8)$$

Here T_b is set to 5°C as that in Murray et al. (1989). [Similar to the approach outlined in Kim et al. \(2015\), the](#) onset of greenness is triggered if the GDD exceeds a threshold value G_b and a temperature-dependent phenological factor f_T is calculated as follows:

$$f_T = \begin{cases} \min\left(1, \frac{GDD - G_b}{L_g}\right), & \text{if } GDD \geq G_b \\ 0, & \text{otherwise} \end{cases} \quad (9)$$

Following Murray et al. (1989), the threshold $G_b = a + b \exp(r \cdot NCD)$ is dependent on the number of chill days (NCD), which is calculated as the total days with < 5°C from winter solstice.

The autumn phenology is more uncertain than budburst because it is affected by both temperature and photoperiod (White et al., 1997; Delpierre et al., 2009). For the

Xu Yue 7/18/15 11:51 AM

Deleted: we have extended the phenology scheme proposed by

Xu Yue 7/18/15 11:51 AM

Deleted: Kim and Wang (2005)

Xu Yue 7/18/15 11:51 AM

Deleted: , based on

Xu Yue 7/18/15 11:52 AM

Deleted: The

temperature dependent phenology, we adopted the cumulative cold summation method (Dufrene et al., 2005; Richardson et al., 2006), which calculates the accumulative falling degree day (FDD) for the m th day from summer solstice as follows,

$$FDD = \sum_{i=1}^m \min(T_{10} - T_s, 0) \quad (10)$$

where T_s is 20°C as that in Dufrene et al. (2005). Similar to the budburst process, we determine autumn phenological factor based on a fixed threshold F_s :

$$f_T = \begin{cases} \max\left(0, 1 + \frac{FDD - F_s}{L_f}\right), & \text{if } FDD \leq F_s \\ 1, & \text{otherwise} \end{cases} \quad (11)$$

In addition, we assume photoperiod regulates leaf senescence as follows,

$$f_P = \begin{cases} \max\left(0, \frac{P - P_i}{P_x - P_i}\right), & \text{if } P \leq P_x \\ 1, & \text{otherwise} \end{cases} \quad (12)$$

where f_P is the photoperiod-limited phenology. P is daylength in minutes. P_i and P_x are the lower and upper limits of daylength for the period of leaf fall. Finally, the autumn phenology of DBF is determined as the product of f_T (Equation 11) and f_P (Equation 12). Both the spring and autumn phenology schemes have been evaluated with extensive ground records over the U.S. in Y2015.

3.2.2 Shrubland

Shrub phenology is sensitive to temperature and/or water availability. We calculate correlation coefficients between observed GPP and soil meteorology at 18 shrub sites (Fig. 2). For 10 sites with annual mean soil temperature < 9 °C, the GPP-temperature correlations are close to 1 while the GPP-moisture correlations are all negative (Fig. 2a),

suggesting that temperature is the dominant phenological driver for these plants. In contrast, for 8 sites with average soil temperature $> 14^{\circ}\text{C}$, GPP-moisture correlations are positive and usually higher than the GPP-temperature correlations, indicating that phenology is primarily regulated by water availability at climatologically warm areas. The wide temperature gap ($9\text{-}14^{\circ}\text{C}$) is due to the limit in the availability of shrub sites. Here, we select a tentative threshold of 12°C to distinguish cold and drought species. We also try to identify phenological drivers based on soil moisture thresholds but find that both temperature- and drought-dependent phenology may occur at moderately dry conditions (Fig. 2b).

In the model, we apply the temperature-dependent phenology f_T for shrubland, if the site has annual mean soil temperature $< 12^{\circ}\text{C}$. We use the same f_T as that for DBF (Equations 9 and 11), due to the lack of long-term phenology measurements at the shrub sites. However, if the soil temperature is $> 12^{\circ}\text{C}$, the plant growth is controlled by drought-limit phenology f_D instead:

$$f_D = \begin{cases} \max\left(0, \frac{\beta_{10} - \beta_{\min}}{\beta_{\max} - \beta_{\min}}\right), & \text{if } \beta_{10} \leq \beta_{\max} \\ 1, & \text{otherwise} \end{cases} \quad (13)$$

where β_{10} is 10-day average water stress calculated based on soil moisture, soil ice fraction, and root fraction of each soil layer (Porporato et al., 2001). The value of β_{10} changes from 0 to 1, with lower value indicating drier soil. Two thresholds, β_{\max} and β_{\min} , represent the upper and lower thresholds that trigger the drought limit for woody species. The values of these thresholds are set to $\beta_{\max} = 1$ and $\beta_{\min} = 0.4$ so that the predicted phenology has the maximum correlations with the observed GPP seasonality (Fig. S1a). The shrub phenology applies for shrubland in tropical and subtropical areas, as well as tundra at the subarctic regions, though the phenology of the latter is usually dependent on temperature alone because the climatological soil temperature is $< 12^{\circ}\text{C}$.

3.2.3 Grassland

In the model, we consider temperature-dependent phenology for grassland based on soil temperature (ST) accumulation (White et al., 1997):

$$SGDD = \sum_{i=1}^n \max(ST_{10} - ST_b, 0) \quad (14)$$

where ST_{10} is 10-day average soil temperature and $ST_b = 0$ °C. Similar to DBF, the onset of grass greenness is triggered if $SGDD$ is higher than a threshold value SG_b (Kim et al., 2015):

$$f_T = \begin{cases} \min\left(1, \frac{SGDD - SG_b}{SL_g}\right), & \text{if } SGDD \geq SG_b \\ 0, & \text{otherwise} \end{cases} \quad (15)$$

where SL_g determines the grow length of grass. Both SG_b and SL_g are calibrated based on observed GPP seasonality at FLUXNET sites (Table 2). Grass phenology at warm sites is also sensitive to water stress (Fig. 2c). We apply the same drought-limit phenology f_D as shrubland (Equation 13) for grassland but with calibrated threshold $\beta_{\max} = 0.9$ and $\beta_{\min} = 0.3$ (Fig. S1b). Different from shrubland whose phenology is dominated by drought when $ST > 12$ °C (Fig. 2a), grassland phenology is jointly affected by temperature and soil moisture (Fig. 2c). As a result, the final phenology for grassland at warm regions is the minimum of f_T and f_D .

3.2.4 Other PFTs

YIBs considers two evergreen PFTs, ENF at high latitudes and EBF in tropical areas. Observations do suggest that evergreen trees experience seasonal changes in LAI, following temperature variations and/or water availability (Doughty and Goulden, 2008; Schuster et al., 2014). However, due to the large uncertainty of evergreen phenology, we set a constant phenology factor of 1.0 for these species, following the approach adopted in other process-based vegetation models (Bonan et al., 2003; Sitch et al., 2003). We implement a parameterization for the impact of cold temperature (frost hardening) on the

maximum carboxylation capacity (V_{cmax}) so as to reduce cold injury for ENF during winter (Hanninen and Kramer, 2007). EBF may experience reduced photosynthesis during the dry season through the effects of water stress on stomatal conductance (Jones et al., 2014).

Crop phenology depends on planting and harvesting dates. In YIBs, we apply a global dataset of crop planting and harvesting dates (Sacks et al., 2010; Unger et al., 2013). Crop budburst occurs at the plant date and the crop continues to grow for a period of 30 days until reaching full maturity ($f = 1$). The crop leaves begin to fall 15 days prior to the harvest date, after which phenology is set to 0. A similar treatment has been adopted in CLM model (Bonan et al., 2003). Thus, crop productivity but not crop phenology is sensitive to the imposed meteorological forcings.

3.3 Carbon allocation

We adopt the autotrophic respiration and carbon allocation scheme applied in the dynamic global vegetation model (DGVM) TRIFFID (Cox, 2001; Clark et al., 2011). On a daily basis, the plant LAI is updated as follows:

$$LAI = f \cdot LAI_b \quad (16)$$

where f is the phenological factor, and LAI_b is the biomass-balanced (or available maximum) LAI related to tree height. LAI_b is dependent on the vegetation carbon content C_{veg} , which is the sum of carbon from leaf (C_l), root (C_r), and stem (C_w):

$$C_{veg} = C_l + C_r + C_w \quad (17)$$

where each carbon component is a function of LAI_b :

$$C_l = \sigma_l \cdot LAI \quad (18a)$$

$$C_r = \sigma_r \cdot LAI_b \quad (18b)$$

$$C_w = a_{wl} \cdot LAI^{b_{wl}} \quad (18c)$$

here σ_l is the specific leaf carbon density. a_{wl} and b_{wl} are PFT-specified allometric parameters (Table 1). The vegetation carbon content C_{veg} is updated every 10 days based on the carbon balance of assimilation, respiration, and litter fall.

$$\frac{dC_{veg}}{dt} = (1 - \lambda) \cdot NPP - \Lambda_l \quad (19)$$

The net primary productivity (NPP) is the net carbon uptake:

$$NPP = GPP - R_a \quad (20)$$

here GPP is the total photosynthesis rate integrated over LAI. Autotrophic respiration (R_a) is split into maintenance (R_{am}) and growth respiration (R_{ag}) (Clark et al., 2011):

$$R_a = R_{am} + R_{ag} \quad (21)$$

The maintenance respiration is calculated based on nitrogen content in leaf (N_l), root (N_r), and stem (N_w) as follows,

$$R_{am} = 0.012 R_d \left(\beta + \frac{N_r + N_w}{N_l} \right) \quad (22)$$

where R_d is the dark respiration of leaf, which is dependent on leaf temperature and is integrated over whole canopy LAI. The factor of 0.012 is the unit conversion from mol CO₂ m⁻² s⁻¹ to kg C m⁻² s⁻¹ and β is water stress representing soil water availability. The nitrogen contents are given by:

$$N_l = n_0 \cdot C_l \quad (23a)$$

$$N_r = n_{rl} \cdot n_0 \cdot C_r \quad (23b)$$

$$N_w = n_{wl} \cdot n_0 \cdot \eta \cdot H \cdot LAI \quad (23c)$$

423

424 here n_0 is leaf nitrogen concentration, n_{rl} and n_{wl} are ratios of nitrogen concentrations of
 425 root and stem to leaves, η is a factor scaling live stem mass to LAI and tree height H . We
 426 adopt the same values of n_0 , n_{rl} , n_{wl} and η as that of TRIFFID model (Table 1) except that
 427 n_{rl} is set to 0.5 following observations of deciduous trees by Sugiura and Tatenno (2011).
 428 The growth respiration is dependent on the residual between GPP and R_{am} based on a
 429 ratio r_g set to 0.2 for all PFTs (Knorr, 2000):

430

$$R_{ag} = r_g \cdot (GPP - R_{am}) \quad (24)$$

432

433 The λ in Equation (19) is a partitioning coefficient determining the fraction of NPP used
 434 for spreading:

435

$$\lambda = \begin{cases} 1, & \text{if } LAI_b > LAI_{\max} \\ \frac{LAI_b - LAI_{\min}}{LAI_{\max} - LAI_{\min}}, & \text{if } LAI_{\min} \leq LAI_b \leq LAI_{\max} \\ 0, & \text{if } LAI_b < LAI_{\min} \end{cases} \quad (25)$$

437

438 where LAI_{\min} and LAI_{\max} are minimum and maximum LAI values for a specific PFT
 439 (Table 1). In the current model version, we turn off the fractional changes by omitting
 440 λNPP in the carbon allocation but feeding it as input for the soil respiration. The litter fall
 441 rate Λ_l in Equation (19) consists of contributions from leaf, root, and stem as follows,

442

$$\Lambda_l = \gamma_l \cdot C_l + \gamma_r \cdot C_r + \gamma_w \cdot C_w \quad (26)$$

444

445 here γ_l , γ_r , and γ_w are turnover rate (yr^{-1}) for leaf, root, and stem carbon respectively.
 446 The leaf turnover rate is calculated based on the phenology change every day. The root
 447 and stem turnover rates are PFT-specific constants (Table 1), derived based on the meta-

analysis by Gill and Jackson (2000) for root and Stephenson and van Mantgem (2005) for stem.

3.4 Soil respiration

The soil respiration scheme is developed based on the Carnegie-Ames-Stanford Approach (CASA) model (Potter et al., 1993; Schaefer et al., 2008), which considers carbon flows among 12 biogeochemical pools. Three live pools, including leaf C_l , root C_r , and wood C_w , contain biomass carbon assimilated from photosynthesis. Litterfall from live pools decomposes and transits in nine dead pools, which consist of one coarse woody debris (CWD) pool, three surface pools, and five soil pools. The CWD pool is composed of dead trees and woody roots. Both surface and soil have identical pools, namely structural, metabolic, and microbial pools, which are distinguished by the content and functions. The structural pool contains lignin, the metabolic pool contains labile substrates, and the microbial pool represents microbial populations. The remaining two soil pools, the slow and passive pools, consist of organic material that decays slowly. The full list of carbon flows among different pools has been illustrated by Schaefer et al. (2008) (c.f. their Fig. 1).

When carbon transfers from pool j to pool i , the carbon loss of pool j is:

$$L_{j2i} = f_{j2i} k_j C_j \quad (27)$$

where C_j is the carbon in pool j , k_j is the total carbon loss rate of pool j , and f_{j2i} is the fraction of carbon lost from pool j transferred to pool i . The coefficient k_j is dependent on soil temperature, moisture, and texture. Meanwhile, the carbon gain of pool i is:

$$G_{j2i} = e_{j2i} \cdot L_{j2i} = e_{j2i} f_{j2i} k_j C_j \quad (28)$$

where e_{j2i} is the ratio of carbon received by pool i to the total carbon transferred from pool j . The rest of the transferred carbon is lost due to heterotrophic respiration:

$$R_{j2i} = (1 - e_{j2i}) \cdot L_{j2i} \quad (29)$$

As a result, the carbon in the i th pool is calculated as

$$\frac{dC_i}{dt} = \sum_{j=1}^n G_{j2i} - \sum_{k=1}^m L_{i2k} \quad (30)$$

The total heterotrophic respiration (R_h) is the summation of R_{j2i} for all pair pools where carbon transitions occur. The total soil carbon is the summation of carbon for all dead pools:

$$C_{soil} = \sum_{i=1}^9 C_i \quad (31)$$

The net ecosystem productivity (NEP) is calculated as

$$NEP = -NEE = NPP - R_h = GPP - R_a - R_h \quad (32)$$

where NEE is the net ecosystem exchange, representing net carbon flow from land to atmosphere. YIBs does not yet account for NEE perturbations due to dynamic disturbance.

3.5 Ozone vegetation damage effects

We apply the semi-mechanistic parameterization proposed by Sitch et al. (2007) to account for ozone damage to photosynthesis through stomatal uptake. The scheme simulates associated changes in both photosynthetic rate and stomatal conductance. When photosynthesis is inhibited by ozone, stomatal conductance decreases accordingly to resist more ozone molecules. We employed an off-line regional version of YIBs to show that present-day ozone damage decreases GPP by 4-8% on average in the eastern U.S. and leads to larger decreases of 11-17% in east coast hotspots (Yue and Unger,

2014). In the current model version, the photosynthesis and stomatal conductance responses to ozone damage are coupled. In future work, we will update the ozone vegetation damage function in YIBs to account for decoupled photosynthesis and stomatal conductance responses based on recent extensive meta-data analyses (Wittig et al., 2007; Lombardozzi et al., 2013).

3.6 Biogenic volatile organic compound (BVOC) emissions

YIBs incorporates two independent leaf-level isoprene emission schemes embedded within the exact same host model framework (Zheng et al., 2015). The photosynthesis-based isoprene scheme simulates emission as a function of the electron transport-limited photosynthesis rate (J_e , Equation 3), canopy temperature, intercellular CO_2 (c_i) and Γ^* (Arneth et al., 2007; Unger et al., 2013). The MEGAN scheme applies the commonly used leaf-level functions of light and canopy temperature (Guenther et al., 1993; Guenther et al., 1995; Guenther et al., 2012). Both isoprene schemes account for atmospheric CO_2 -sensitivity (Arneth et al., 2007). Long-term increases (decreases) in atmospheric CO_2 decrease (increase) isoprene emissions (Unger et al., 2013). The CO_2 -sensitivity is higher under lower atmospheric CO_2 levels than present day. Leaf-level monoterpene emissions are simulated using a simplified temperature dependent algorithm (Lathiere et al., 2006). The leaf-level isoprene and monoterpene emissions are integrated over the multiple canopy layers in the exact same way as GPP to obtain the total canopy-level emissions.

3.7 Implementation of YIBs into NASA ModelE2 (NASA ModelE2-YIBs)

NASA ModelE2 has a spatial resolution of $2^\circ \times 2.5^\circ$ latitude by longitude with 40 vertical levels extending to 0.1 hPa. In the on-line configuration, the global climate model provides the meteorological drivers to YIBs and the land-surface hydrology submodel provides the soil characteristics (Rosenzweig and Abramopoulos, 1997; Schmidt et al., 2014). Recent relevant updates to NASA ModelE2 include a dynamic fire activity parameterization from Pechony and Shindell (2009) and climate-sensitive soil NO_x emissions based on Yienger and Levy (1995) (Unger and Yue, 2014). Without the YIBs implementation, the default NASA ModelE2 computes dry deposition using fixed LAI

and vegetation cover fields from Olson et al. (2001), which are different from the climate model's vegetation scheme (Shindell et al., 2013b). With YIBs embedded in NASA ModelE2, the YIBs model provides the vegetation cover and LAI for the dry deposition scheme. The on-line simulated atmospheric ozone and aerosol concentrations influence terrestrial carbon assimilation and stomatal conductance at the 30-minute integration time step. In turn, the on-line vegetation properties, and water, energy and BVOC fluxes affect air quality, meteorology and the atmospheric chemical composition. The model simulates the interactive deposition of inorganic and organic nitrogen to the terrestrial biosphere. However, the YIBs biosphere currently applies fixed nitrogen levels and does not yet account for the dynamic interactions between the carbon and nitrogen cycles, and the consequences for carbon assimilation, which are highly uncertain (e.g., Thornton et al., 2007; Koven et al., 2013; Thomas et al., 2013; Zaehle et al., 2014; Houlton et al., 2015).

4. Model setup and simulations

4.1 Site-level simulations (YIBs-site)

We perform site-level simulations with offline YIBs model at 145 eddy covariance flux tower sites for the corresponding PFTs (Fig. 1). Hourly *in situ* measurements of meteorology (Sect. 2.1) are used as input for the model. We gap filled missing measurements with the Global Modeling and Assimilation Office (GMAO) Modern Era-Retrospective Analysis (MERRA) reanalysis (Rienecker et al., 2011), as described in Yue and Unger (2014). All grasslands and most croplands are considered as C3 plants, except for some sites where corn is grown. Meteorological measurements are available for a wide range of time periods across the different sites ranging from the minimum of 1 year at some sites (e.g. BE-Jal) and the maximum of 16 years at Harvard Forest (US-HA1). The soil carbon pool initial conditions at each site are provided by the 140-year spin up procedure using YIBs-offline (Supplement). An additional 30-year spin up is conducted for each site-level simulation using the initial height H_0 for corresponding PFT (Table 1) and the fixed meteorology and CO₂ conditions at the first year of observations. Then, the simulation is continued with year-to-year forcings at the specific site for the rest of measurement period. For all grass and shrub sites, two simulations are performed. One

applies additional drought controls on phenology as described in Sects. 3.2.2 and 3.2.3, while the other uses only temperature-dependent phenology. By comparing results of these two simulations, we assess the role of drought phenology for plants in arid and semi-arid regions.

4.2 Global off-line simulation (YIBs-offline)

The global off-line YIBs applies the CLM land cover dataset (Oleson et al., 2010). Land cover is derived based on retrievals from both MODIS (Hansen et al., 2003) and AVHRR (Defries et al., 2000). Fractions of 16 PFTs are aggregated into 9 model PFTs (Table 1). The soil carbon pool and tree height initial conditions are provided by the 140-year spin up procedure using YIBs-offline (Supplement). The global off-line YIBs model is driven with WFDEI meteorology (Weedon et al., 2014) at $1^\circ \times 1^\circ$ horizontal resolution for the period of 1980-2011. Observed atmospheric CO₂ concentrations are adopted from the fifth assessment report (AR5) of the Intergovernmental Panel on Climate Change (IPCC) (Meinshausen et al., 2011). We evaluate the simulated long-term 1980-2011 average tree height/LAI and carbon fluxes with available observations and recent multi-model inter-comparisons. Attribution of the decadal trends in terrestrial carbon fluxes are explored in a separate follow-on companion study (Yue et al., 2015b).

4.3 Global on-line simulation in NASA ModelE2-YIBs

The global land cover data is identical to that used in YIBs-offline (Sect. 4.2) based on the CLM cover. Because our major research goal is to study short-term (seasonal, annual, decadal) interactions between vegetation physiology and atmospheric chemistry, we elect to prescribe the PFT distribution in different climatic states. We perform an on-line atmosphere-only simulation representative of the present day (~2000s) climatology by prescribing fixed monthly-average sea surface temperature (SST) and sea ice temperature for the 1996-2005 decade from the Hadley Center as the boundary conditions (Rayner et al., 2006). Atmospheric CO₂ concentration is fixed at the level of the year 2000 (370 ppm). In NASA ModelE2-YIBs, initial conditions for soil carbon pools and tree heights are provided by the 140-year spin-up process described in the Supplement using YIBs-offline but for year 2000 (not 1980) fixed WFDEI meteorology and atmospheric CO₂

conditions. The NASA ModelE2-YIBs global carbon-chemistry-climate model is run for an additional 30 model years. The first 20 years are discarded as the on-line spin-up and the last 10-year results are averaged for the analyses including comparisons with observations and the YIBs-offline.

4.4 Ozone vegetation damage simulation (YIBs-ozone)

We perform two simulations to quantify ozone vegetation damage with the off-line YIBs model based on the high and low ozone sensitivity parameterizations (Sitch et al., 2007). Similar to the set up in Yue and Unger (2014), we use off-line hourly surface ozone concentrations simulated with the NASA ModelE2 based on the climatology and precursor emissions of the year 2000 (Sect. 4.3). In this way, atmospheric ozone photosynthesis damage affects plant growth, including changes in tree height and LAI. We compare the simulated ozone damage effects with the previous results in Yue and Unger (2014) that used prescribed LAI. For this updated assessment, we do not isolate possible feedbacks from the resultant land carbon cycle changes to the surface ozone concentrations themselves, for instance through concomitant changes to BVOC emissions and water fluxes. The importance of these feedbacks will be quantified in future research using the on-line NASA ModelE2-YIBs framework.

5. Results

5.1 Site-level evaluation

The simulated monthly-average GPP is compared with measurements at 145 sites for different PFTs (Fig. 3). GPP simulation biases range from -19% to 7% depending on PFT. The highest correlation of 0.86 is achieved for DBF, mainly contributed by the reasonable phenology simulated at these sites (Fig. S2). The correlation is also high for ENF sites even though phenology is set to a constant value of 1.0. A relatively low correlation of 0.65 is modeled for EBF sites (Fig. S2). However, the site-specific evaluation shows that the simulations reasonably capture the observed magnitude and seasonality, including the minimum GPP in summer due to drought at some sites (e.g. FR-Pue and IT-Lec). Predictions at crop sites achieve a medium correlation of 0.77,

because the prescribed crop phenology based on the planting and harvesting dates dataset matches reality for most sites with some exceptions (e.g. CH-Oe2). Measured GPP at shrub and grass sites show varied seasonality. For most sites, the maximum carbon fluxes are measured in the hemispheric summer season. However, for sites with arid or Mediterranean climate, the summer GPP is usually the lowest during the year (e.g. ES-LMa and US-Var in Fig. S2) while the peak flux is observed during the wet season when the climate is cooler and moister. Implementing the drought-dependent phenology helps improve the GPP seasonality and decrease the root-mean-square error (RMSE) at most warm climate shrub and grass sites (Fig. S3).

A synthesis of the site-level evaluation is presented in Fig. 4. Among the 145 sites, 121 have correlations higher than 0.8 for the GPP simulation (Fig. 4a). Predictions are better for PFTs with larger seasonal variations. For example, high correlations of >0.8 are achieved at 95% ENF and DBF sites, but only 70% for grass and 45% for EBF sites. Low relative biases (-33% - 50%) are achieved at 94 sites (Fig. 4b). For most PFTs, a similar fraction (65%) of the sites have low biases falling into that range, except for cropland, where only 7 sites (45%) have the low biases. The RMSE is lower than 3 g [C] day^{-1} for 107 out of 145 sites (Fig. 4c). The highest RMSE is predicted for crop sites, where the model misses the large interannual variations due to crop rotation at some sites (e.g. BE-Lon, DE-Geb, and US-Ne2). YIBs model performs simulations at the PFT level while measurements show large uncertainties in the carbon fluxes among biomes/species within the same PFT (Luyssaert et al., 2007). The simulated intraspecific variations (in the form of standard deviation) are smaller than the measured/derived values for most PFTs (Table S2), likely because of the application of fixed photosynthetic parameters for each PFT (Table 1).

Compared with GPP, the NEE simulations have smaller correlations with measurements because of the limited seasonality in the observations at most sites (Fig. S4). 74 sites (51%) have correlation coefficients higher than 0.6 (Fig. 4d) and 75 sites (52%) have absolute biases within $\pm 0.5 \text{ g [C] day}^{-1}$ (Fig. 4e). For most ENF sites, the maximum net carbon uptake (the minimum NEE) is observed in spring or early summer, when GPP

begins to increase while soil respiration is still at low rate due to the cool and wet conditions (e.g. CA-Ojp and ES-ES1). Compared with other PFTs, the DBF trees usually have larger seasonality with the NEE peak in the early summer. Such seasonality helps promote correlations between model and measurements, resulting in high R (>0.8) for 17 out of 20 sites (Fig. 4d). For shrub and grass sites, the observed seasonality of NEE is not regular, though most show maximum carbon uptake in spring or early summer. Implementation of drought-dependent phenology helps improve the simulated NEE seasonality at some sites of these PFTs (e.g. ES-LMa and IT-Pia), however, such improvement is limited for others (Fig. S4). Simulated crop NEE reaches maximum magnitude in summer at most sites, consistent with observations and leading to a high R (> 0.8) for 10 out 16 sites (Fig. 4d). The RMSE of simulated NEE is larger for crop relative to other PFTs because the model does not treat crop rotation (Fig. 4f).

5.2 Evaluation of YIBs-offline

YIBs-offline forced with WFDEI meteorology simulates reasonable spatial distributions for tree height, LAI, and GPP, all of which show maximums in the tropical rainforest biome and medium values in the Northern Hemisphere high latitudes (Fig. 5). Compared with the satellite observations, the simulated height is underestimated by 30% on the annual and global mean basis (Fig. 5b). Regionally, the prediction is larger by only 4% for tropical rainforest and temperate DBF, but by 27% for boreal ENF, for which the model assumes a constant phenology of 1.0 all the year round. However, for the vast areas covered with grass and shrub PFTs, the simulated height is lower by 41% with maximum underestimation in Eastern Siberia, where the model land is covered by short tundra. The modeled LAI is remarkably close to observations on the annual and global mean basis (Figs. 5c-d). However, there are substantial regional biases in model LAI. Model LAI prediction is higher by $0.8 \text{ m}^2 \text{ m}^{-2}$ (70%) for boreal ENF and by $0.1 \text{ m}^2 \text{ m}^{-2}$ (5%) for tropical rainforest. In contrast, the simulation underestimates LAI of tropical C4 grass by $0.4 \text{ m}^2 \text{ m}^{-2}$ (30%) and shrubland by $0.2 \text{ m}^2 \text{ m}^{-2}$ (30%). The GPP simulation is lower than the FLUXNET-derived value by 5% on the global scale, which is contributed by the minor underestimation for all PFTs except for tropical rainforest, where model predicts 9% higher GPP than observations (Fig. 5f).

693

694 The model simulates reasonable seasonality for LAI and land carbon fluxes (Fig. 6). Tree
695 height shows limited seasonal variations, especially for DBF, ENF, and EBF trees. LAI,
696 GPP, and NPP also exhibit small seasonality over tropical areas, such as the Amazon,
697 Central Africa, and Indonesia. However, for temperate areas, such as North America,
698 Europe and East Asia, these variables show large seasonal variations with minimum in
699 winter and maximum in summer. The LAI is overestimated by 20% in Amazon during
700 the December-January-February season but underestimated by 25% in Indonesia during
701 summer (Fig. 6b). For GPP and NPP, the positive bias in Indonesia is even larger at 45%
702 during summer (Figs. 6c-d).

703

704 On the global scale, YIBs-offline simulates GPP of $124.6 \pm 3.3 \text{ Pg C a}^{-1}$ and NEE of -2.5
705 $\pm 0.7 \text{ Pg C a}^{-1}$ for 1982-2011. These values are consistent with estimates upscaled from
706 the FLUXNET observations (Jung et al., 2009; Friedlingstein et al., 2010; Jung et al.,
707 2011) and simulations from 10 other carbon cycle models (Piao et al., 2013) (Fig. 7). The
708 net biome productivity (NBP) is in opposite sign to NEE. Tropical areas (23°S - 23°N)
709 account for 63% of the global GPP, including 27% from Amazon rainforest, 21% from
710 central Africa, and 5% from Indonesia forest (Table 3). A lower contribution of 57%
711 from tropics is predicted for both NPP and heterotrophic respiration. However, for NEE,
712 only 40% of the land carbon sink is contributed by tropical forests and grasslands, while
713 56% is from temperate forests and grasslands in North America, Europe, and East Asia.

714

715 We compare the simulated budburst dates with observations from satellite retrieval (Fig.
716 8). The model captures the basic spatial pattern of spring phenology with earlier to later
717 budburst dates from lower to higher latitudes. On average, the observed budburst date in
718 Northern Hemisphere (NH) is 133 DOY (May 13th) and simulation is 132 DOY (May
719 12th). Such close estimate results from the regional delay of 10 days (119 versus 129
720 DOY) in Europe and advance of 4 days (140 versus 136 DOY) in East Asia. In Y2015,
721 extensive (~75000 records) ground-based measurements have been used to validate the
722 simulated spring and autumn phenology in U.S. and both the spatial distribution and
723 interannual variation of simulation are reasonable.

5.3 Evaluation of NASA ModelE2-YIBs

NASA ModelE2-YIBs simulations of global land carbon fluxes show similar spatial distribution and magnitude as the YIBs-offline model (Figs. S6-S8). However, due to differences in the meteorological forcings (Figs. S9-S12), regional discrepancies between the two configurations occur. The predicted LAI with NASA ModelE2-YIBs is lower by 20% in Amazon region than YIBs-offline (Fig. S6), following the similar magnitude of differences in regional GPP and NPP (Figs. S7-S8). We performed driver attribution sensitivity simulations, in which the YIBs-offline configuration is driven with the same meteorological forcings simulated by NASA ModelE2 except for one selected field from the WFDEI reanalysis. We found that the anomalously warmer climate over the Amazon in the global climate model (Fig. S9) causes the lower GPP in that region in NASA ModelE2-YIBs. The temperature optimum for C3 photosynthesis is around 30 °C, above which the maximum rate of electron transport (Equation 3) decreases dramatically (Farquhar et al., 1980). As a result, the higher NASA ModelE2-YIBs surface temperature in the tropical rainforest results in the lower photosynthesis rates there. With the exception of the Amazon, the NASA ModelE2-YIBs June-July-August GPP and NPP show low biases in central Africa and high latitudes in North America and Asia, but high biases in Europe, western U.S., and eastern China (Figs. S7-S8). The sensitivity tests attribute these discrepancies to differences in canopy humidity (Fig. S11) and soil wetness (Fig. S12). Low soil wetness decreases water stress β , reduces the slope m of Ball-Berry equation (Equation 6), and consequently limits photosynthesis by declining stomatal conductance in combination with low humidity. On the global scale, the ModelE2-YIBs simulates annual GPP of 122.9 Pg C, NPP of 62 Pg C, and NEE of -2.7 Pg C, all of which are close to the YIBs-offline simulation (Table 3) and consistent with results from observations and model inter-comparison (Fig. 7).

5.4 Assessment of global ozone vegetation damage

Ozone dampens GPP and consequently affects tree growth and LAI. In North America, the annual average reductions range from 2% to 6%, depending on the plant sensitivity to

ozone damage (Table 3). Locally, average damages reach as high as 5-11% in the eastern U.S. with maximums up to 11-23% (Figs. 9a-b). These values are higher than the estimate of 4-8% (maximum 11-17%) by Yue and Unger (2014), because the latter used prescribed LAI in the simulation and did not consider the LAI reductions due to ozone damage (Figs. 9c-d). The YIBs model predicts similar magnitude of damages in Europe compared to North America, but almost doubled effects in East Asia (Table 3) due to the high ozone concentrations there, especially in boreal summer (Fig. S5). Ozone-induced GPP-reductions are limited in tropical areas (Fig. 5e) because the surface ozone levels there are very low, for example, especially over the Amazon forest (Fig. S5). The damage to LAI generally follows the pattern of GPP reductions but the response signal is weaker than that of GPP (Figs. 9c-d).

6. Conclusions and discussion

We describe and evaluate the process-based YIBs interactive terrestrial biosphere model. YIBs is embedded into the NASA ModelE2 global chemistry-climate model and is an important urgently needed development to improve the biological realism of interactions between vegetation, atmospheric chemistry and climate. We implement both temperature- and drought-dependent phenology for DBF, shrub, and grass species. The model simulates interactive ozone vegetation damage. The YIBs model is fully validated with land carbon flux measurements from 145 ground stations and global observations of canopy height, LAI, GPP, NPP, and phenology from multiple satellite retrievals.

There are several limitations in the current model set up. The vegetation parameters, V_{cmax} , m , and b (Table 1), are fixed at the PFT level, which may induce uncertainties in the simulation of carbon fluxes due to intraspecific variations (Kattge et al., 2011). The model does not yet include a dynamic treatment of nitrogen and phosphorous availability because current schemes suffer from large uncertainties (Thornton et al., 2007; Zaehle et al., 2014; Houlton et al., 2015). Phenology is set to a constant value of 1 for ENF and EBF, which is not consistent with observations (O'Keefe, 2000; Jones et al., 2014). The ozone damage scheme of Sitch et al. (2007) considers coupled responses of

photosynthesis and stomatal conductance while observations suggest a decoupling (Lombardozzi et al., 2013).

Despite these limitations, the YIBs model reasonably simulates global land carbon fluxes compared with both site-level flux measurements and global satellite observations. YIBs is primed for on-going development, for example, incorporating community dynamics including mortality, establishment, seed transport and dynamic fire disturbance (Moorcroft et al., 2001). NASA ModelE2-YIBs is available to be integrated with interactive ocean and atmospheric carbon components to offer a full global carbon-climate model, for example for use in interpreting and diagnosing new satellite datasets of atmospheric CO₂ concentrations. In the current form, NASA ModelE2-YIBs provides a useful new tool to investigate the impacts of air pollution on the carbon budget, water cycle, and surface energy balance, and, in turn, the impacts of changing vegetation physiology on the atmospheric chemical composition. Carbon-chemistry-climate interactions, a relatively new interdisciplinary research frontier, are expected to influence the evolution of the Earth's climate system on multiple spatiotemporal scales.

Code availability

The YIBs model (version 1.0) site-level source code is available at https://github.com/YIBS01/YIBS_site. The source codes for the global off-line and global on-line versions of the YIBs model (version 1.0) are available through collaboration. Please submit request to X. Yue (xu.yue@yale.edu) and N. Unger (nadine.unger@yale.edu). Auxiliary forcing data and related input files must be obtained independently.

Acknowledgements. Funding support for this research is provided by the NASA Atmospheric Composition Campaign Data Analysis and Modeling Program. This project was supported in part by the facilities and staff of the Yale University Faculty of Arts and Sciences High Performance Computing Center. [We are grateful to Y. Kim, I. Aleinov, and N. Y. Kiang for access to unpublished codes.](#) We thank Ranga B. Myneni and

818 Zaichun Zhu for providing the AVHRR LAI3g dataset.

819 **References**

- 820 Ainsworth, E. A., Yendrek, C. R., Sitch, S., Collins, W. J., and Emberson, L. D.: The
821 effects of tropospheric ozone on net primary productivity and implications for climate
822 change, *Annu Rev Plant Biol*, 63, 637-661, doi:10.1146/Annurev-Arplant-042110-
823 103829, 2012.
- 824 Arneth, A., Niinemets, U., Pressley, S., Back, J., Hari, P., Karl, T., Noe, S., Prentice, I.
825 C., Serca, D., Hickler, T., Wolf, A., and Smith, B.: Process-based estimates of
826 terrestrial ecosystem isoprene emissions: incorporating the effects of a direct CO₂-
827 isoprene interaction, *Atmos Chem Phys*, 7, 31-53, doi:10.5194/acp-7-31-2007, 2007.
- 828 Baldocchi, D.: An Analytical Solution for Coupled Leaf Photosynthesis and Stomatal
829 Conductance Models, *Tree Physiol*, 14, 1069-1079, 1994.
- 830 Ball, J. T., Woodrow, I. E., and Berry, J. A.: A model predicting stomatal conductance
831 and its contribution to the control of photosynthesis under different environmental
832 conditions. In: *Progress in Photosynthesis Research*, Biggins, J. (Ed.), Nijhoff,
833 Dordrecht, Netherlands, 221-224, 1987.
- 834 Beer, C., Reichstein, M., Tomelleri, E., Ciais, P., Jung, M., Carvalhais, N., Rodenbeck,
835 C., Arain, M. A., Baldocchi, D., Bonan, G. B., Bondeau, A., Cescatti, A., Lasslop, G.,
836 Lindroth, A., Lomas, M., Luyssaert, S., Margolis, H., Oleson, K. W., Rouspard, O.,
837 Veenendaal, E., Viovy, N., Williams, C., Woodward, F. I., and Papale, D.: Terrestrial
838 Gross Carbon Dioxide Uptake: Global Distribution and Covariation with Climate,
839 *Science*, 329, 834-838, doi:10.1126/Science.1184984, 2010.
- 840 Berry, J. A., Beerling, D. J., and Franks, P. J.: Stomata: key players in the earth system,
841 past and present, *Curr Opin Plant Biol*, 13, 233-240, doi:10.1016/J.Pbi.2010.04.013,
842 2010.
- 843 Bonan, G. B., Lawrence, P. J., Oleson, K. W., Levis, S., Jung, M., Reichstein, M.,
844 Lawrence, D. M., and Swenson, S. C.: Improving canopy processes in the
845 Community Land Model version 4 (CLM4) using global flux fields empirically
846 inferred from FLUXNET data, *J. Geophys. Res.*, 116, G02014,
847 doi:10.1029/2010jg001593, 2011.
- 848 Bonan, G. B., Levis, S., Sitch, S., Vertenstein, M., and Oleson, K. W.: A dynamic global
849 vegetation model for use with climate models: concepts and description of simulated
850 vegetation dynamics, *Global Change Biol*, 9, 1543-1566, doi:10.1046/J.1365-
851 2486.2003.00681.X, 2003.
- 852 Clark, D. B., Mercado, L. M., Sitch, S., Jones, C. D., Gedney, N., Best, M. J., Pryor, M.,
853 Rooney, G. G., Essery, R. L. H., Blyth, E., Boucher, O., Harding, R. J., Huntingford,
854 C., and Cox, P. M.: The Joint UK Land Environment Simulator (JULES), model
855 description - Part 2: Carbon fluxes and vegetation dynamics, *Geosci Model Dev*, 4,
856 701-722, doi:10.5194/Gmd-4-701-2011, 2011.
- 857 Collatz, G. J., Ball, J. T., Grivet, C., and Berry, J. A.: Physiological and Environmental-
858 Regulation of Stomatal Conductance, Photosynthesis and Transpiration - a Model
859 That Includes a Laminar Boundary-Layer, *Agr Forest Meteorol*, 54, 107-136,
860 doi:10.1016/0168-1923(91)90002-8, 1991.
- 861 Collatz, G. J., Ribas-Carbo, M., and Berry, J. A.: Coupled Photosynthesis-Stomatal
862 Conductance Model for Leaves of C₄ Plants, *Aust J Plant Physiol*, 19, 519-538, 1992.
- 863 Cox, P. M.: Description of the "TRIFFID" Dynamic Global Vegetation Model, Hadley
864 Centre technical note 24, 2001.

865 Defries, R. S., Hansen, M. C., Townshend, J. R. G., Janetos, A. C., and Loveland, T. R.:
866 A new global 1-km dataset of percentage tree cover derived from remote sensing,
867 *Global Change Biol*, 6, 247-254, doi:10.1046/J.1365-2486.2000.00296.X, 2000.

868 Delbart, N. and Picard, G.: Modeling the date of leaf appearance in low-arctic tundra,
869 *Global Change Biol*, 13, 2551-2562, doi:10.1111/J.1365-2486.2007.01466.X, 2007.

870 Delpierre, N., Dufrene, E., Soudani, K., Ulrich, E., Cecchini, S., Boe, J., and Francois, C.:
871 Modelling interannual and spatial variability of leaf senescence for three deciduous
872 tree species in France, *Agr Forest Meteorol*, 149, 938-948,
873 doi:10.1016/J.Agrformet.2008.11.014, 2009.

874 Doughty, C. E. and Goulden, M. L.: Seasonal patterns of tropical forest leaf area index
875 and CO₂ exchange, *J. Geophys. Res.*, 113, G00b06, doi:10.1029/2007jg000590,
876 2008.

877 Dufrene, E., Davi, H., Francois, C., le Maire, G., Le Dantec, V., and Granier, A.:
878 Modelling carbon and water cycles in a beech forest Part I: Model description and
879 uncertainty analysis on modelled NEE, *Ecol Model*, 185, 407-436,
880 doi:10.1016/J.Ecolmodel.2005.01.004, 2005.

881 Farquhar, G. D., Caemmerer, S. V., and Berry, J. A.: A Biochemical-Model of
882 Photosynthetic CO₂ Assimilation in Leaves of C-3 Species, *Planta*, 149, 78-90,
883 doi:10.1007/Bf00386231, 1980.

884 Friedlingstein, P., Andrew, R. M., Rogelj, J., Peters, G. P., Canadell, J. G., Knutti, R.,
885 Luderer, G., Raupach, M. R., Schaeffer, M., van Vuuren, D. P., and Le Quere, C.:
886 Persistent growth of CO₂ emissions and implications for reaching climate targets, *Nat*
887 *Geosci*, 7, 709-715, doi:10.1038/Ngeo2248, 2014.

888 Friedlingstein, P., Cox, P., Betts, R., Bopp, L., Von Bloh, W., Brovkin, V., Cadule, P.,
889 Doney, S., Eby, M., Fung, I., Bala, G., John, J., Jones, C., Joos, F., Kato, T.,
890 Kawamiya, M., Knorr, W., Lindsay, K., Matthews, H. D., Raddatz, T., Rayner, P.,
891 Reick, C., Roeckner, E., Schnitzler, K. G., Schnur, R., Strassmann, K., Weaver, A. J.,
892 Yoshikawa, C., and Zeng, N.: Climate-carbon cycle feedback analysis: Results from
893 the (CMIP)-M-4 model intercomparison, *J Climate*, 19, 3337-3353,
894 doi:10.1175/Jcli3800.1, 2006.

895 Friedlingstein, P., Houghton, R. A., Marland, G., Hackler, J., Boden, T. A., Conway, T.
896 J., Canadell, J. G., Raupach, M. R., Ciais, P., and Le Quere, C.: Update on CO₂
897 emissions, *Nat Geosci*, 3, 811-812, doi:10.1038/Ngeo1022, 2010.

898 Friend, A. D. and Kiang, N. Y.: Land surface model development for the GISS GCM:
899 Effects of improved canopy physiology on simulated climate, *J Climate*, 18, 2883-
900 2902, doi:10.1175/Jcli3425.1, 2005.

901 Gill, R. A. and Jackson, R. B.: Global patterns of root turnover for terrestrial ecosystems,
902 *New Phytol*, 147, 13-31, doi:10.1046/J.1469-8137.2000.00681.X, 2000.

903 Guenther, A. B., Hewitt, C. N., Erickson, D., Fall, R., Geron, C., Graedel, T., Harley, P.,
904 Klinger, L., Lerdau, M., McKay, W. A., Pierce, T., Scholes, B., Steinbrecher, R.,
905 Tallamraju, R., Taylor, J., and Zimmerman, P.: A Global-Model of Natural Volatile
906 Organic-Compound Emissions, *J. Geophys. Res.*, 100, 8873-8892,
907 doi:10.1029/94jd02950, 1995.

908 Guenther, A. B., Jiang, X., Heald, C. L., Sakulyanontvittaya, T., Duhl, T., Emmons, L.
909 K., and Wang, X.: The Model of Emissions of Gases and Aerosols from Nature

version 2.1 (MEGAN2.1): an extended and updated framework for modeling biogenic emissions, *Geosci Model Dev*, 5, 1471-1492, doi:10.5194/Gmd-5-1471-2012, 2012.

Guenther, A. B., Zimmerman, P. R., Harley, P. C., Monson, R. K., and Fall, R.: Isoprene and Monoterpene Emission Rate Variability - Model Evaluations and Sensitivity Analyses, *J. Geophys. Res.*, 98, 12609-12617, doi:10.1029/93jd00527, 1993.

Hanninen, H. and Kramer, K.: A framework for modelling the annual cycle of trees in boreal and temperate regions, *Silva Fenn*, 41, 167-205, 2007.

Hansen, M. C., DeFries, R. S., Townshend, J. R. G., Carroll, M., Dimiceli, C., and Sohlberg, R. A.: Global Percent Tree Cover at a Spatial Resolution of 500 Meters: First Results of the MODIS Vegetation Continuous Fields Algorithm, *Earth Interact*, 7, 1-15, doi:10.1175/1087-3562(2003)007<0001:GPTCAA>2.0.CO;2, 2003.

Hollaway, M. J., Arnold, S. R., Challinor, A. J., and Emberson, L. D.: Intercontinental trans-boundary contributions to ozone-induced crop yield losses in the Northern Hemisphere, *Biogeosciences*, 9, 271-292, doi:10.5194/Bg-9-271-2012, 2012.

Houghton, R. A., House, J. I., Pongratz, J., van der Werf, G. R., DeFries, R. S., Hansen, M. C., Le Quere, C., and Ramankutty, N.: Carbon emissions from land use and land-cover change, *Biogeosciences*, 9, 5125-5142, doi:10.5194/Bg-9-5125-2012, 2012.

Houlton, B. Z., Marklein, A. R., and Bai, E.: Representation of nitrogen in climate change forecasts, *Nat Clim Change*, 5, 398-401, 2015.

Huntingford, C., Cox, P. M., Mercado, L. M., Sitch, S., Bellouin, N., Boucher, O., and Gedney, N.: Highly contrasting effects of different climate forcing agents on terrestrial ecosystem services, *Philos T R Soc A*, 369, 2026-2037, doi:10.1098/Rsta.2010.0314, 2011.

Jones, M. O., Kimball, J. S., and Nemani, R. R.: Asynchronous Amazon forest canopy phenology indicates adaptation to both water and light availability, *Environ Res Lett*, 9, 124021, doi:10.1088/1748-9326/9/12/124021, 2014.

Jung, M., Reichstein, M., and Bondeau, A.: Towards global empirical upscaling of FLUXNET eddy covariance observations: validation of a model tree ensemble approach using a biosphere model, *Biogeosciences*, 6, 2001-2013, doi:10.5194/bg-6-2001-2009, 2009.

Jung, M., Reichstein, M., Margolis, H. A., Cescatti, A., Richardson, A. D., Arain, M. A., Arneth, A., Bernhofer, C., Bonal, D., Chen, J. Q., Gianelle, D., Gobron, N., Kiely, G., Kutsch, W., Lasslop, G., Law, B. E., Lindroth, A., Merbold, L., Montagnani, L., Moors, E. J., Papale, D., Sottocornola, M., Vaccari, F., and Williams, C.: Global patterns of land-atmosphere fluxes of carbon dioxide, latent heat, and sensible heat derived from eddy covariance, satellite, and meteorological observations, *J. Geophys. Res.*, 116, G00j07, doi:10.1029/2010jg001566, 2011.

Kattge, J. and co-authors: TRY - a global database of plant traits, *Global Change Biol*, 17, 2905-2935, doi:10.1111/J.1365-2486.2011.02451.X, 2011.

Keenan, T. F., Gray, J., Friedl, M. A., Toomey, M., Bohrer, G., Hollinger, D. Y., Munger, J. W., O'Keefe, J., Schmid, H. P., SueWing, I., Yang, B., and Richardson, A. D.: Net carbon uptake has increased through warming-induced changes in temperate forest phenology, *Nat Clim Change*, 4, 598-604, doi:10.1038/Nclimate2253, 2014.

Kim, Y., Moorcroft, P. R., Aleinov, I., Puma, M. J., and Kiang, N. Y.: Variability of phenology and fluxes of water and carbon with observed and simulated soil moisture

955 in the Ent Terrestrial Biosphere Model (Ent TBM version 1.0.1.0.0), Geosci. Model
 956 Dev. Discuss., in press, 2015.

957 Kim, Y. and Wang, G. L.: Modeling seasonal vegetation variation and its validation
 958 against Moderate Resolution Imaging spectroradiometer (MODIS) observations over
 959 North America, *J. Geophys. Res.*, 110, D04106, doi:10.1029/2004jd005436, 2005.

960 Knorr, W.: Annual and interannual CO₂ exchanges of the terrestrial biosphere: process-
 961 based simulations and uncertainties, *Global Ecol Biogeogr*, 9, 225-252,
 962 doi:10.1046/J.1365-2699.2000.00159.X, 2000.

963 Koch, D., Bauer, S. E., Del Genio, A., Faluvegi, G., McConnell, J. R., Menon, S., Miller,
 964 R. L., Rind, D., Ruedy, R., Schmidt, G. A., and Shindell, D.: Coupled Aerosol-
 965 Chemistry-Climate Twentieth-Century Transient Model Investigation: Trends in
 966 Short-Lived Species and Climate Responses, *J Climate*, 24, 2693-2714,
 967 doi:10.1175/2011jcli3582.1, 2011.

968 Koven, C. D., Riley, W. J., Subin, Z. M., Tang, J. Y., Torn, M. S., Collins, W. D., Bonan,
 969 G. B., Lawrence, D. M., and Swenson, S. C.: The effect of vertically resolved soil
 970 biogeochemistry and alternate soil C and N models on C dynamics of CLM4,
 971 *Biogeosciences*, 10, 7109-7131, doi:10.5194/Bg-10-7109-2013, 2013.

972 Lamarque, J. F., Shindell, D. T., Josse, B., Young, P. J., Cionni, I., Eyring, V.,
 973 Bergmann, D., Cameron-Smith, P., Collins, W. J., Doherty, R., Dalsoren, S.,
 974 Faluvegi, G., Folberth, G., Ghan, S. J., Horowitz, L. W., Lee, Y. H., MacKenzie, I.
 975 A., Nagashima, T., Naik, V., Plummer, D., Righi, M., Rumbold, S. T., Schulz, M.,
 976 Skeie, R. B., Stevenson, D. S., Strode, S., Sudo, K., Szopa, S., Voulgarakis, A., and
 977 Zeng, G.: The Atmospheric Chemistry and Climate Model Intercomparison Project
 978 (ACCMIP): overview and description of models, simulations and climate diagnostics,
 979 *Geosci Model Dev*, 6, 179-206, doi:10.5194/Gmd-6-179-2013, 2013.

980 Lathiere, J., Hauglustaine, D. A., Friend, A. D., De Noblet-Ducoudre, N., Viovy, N., and
 981 Folberth, G. A.: Impact of climate variability and land use changes on global biogenic
 982 volatile organic compound emissions, *Atmos Chem Phys*, 6, 2129-2146,
 983 doi:10.5194/acp-6-2129-2006, 2006.

984 Liu, H., Tian, F., Hu, H. C., Hu, H. P., and Sivapalan, M.: Soil moisture controls on
 985 patterns of grass green-up in Inner Mongolia: an index based approach, *Hydrol Earth*
 986 *Syst Sc*, 17, 805-815, doi:10.5194/Hess-17-805-2013, 2013.

987 Lombardozzi, D., Sparks, J. P., and Bonan, G.: Integrating O₃ influences on terrestrial
 988 processes: photosynthetic and stomatal response data available for regional and global
 989 modeling, *Biogeosciences*, 10, 6815-6831, doi:10.5194/bg-10-6815-2013, 2013.

990 Luyssaert, S. and co-authors: CO₂ balance of boreal, temperate, and tropical forests
 991 derived from a global database, *Global Change Biol*, 13, 2509-2537, doi:Doi
 992 10.1111/J.1365-2486.2007.01439.X, 2007.

993 Mahowald, N.: Aerosol Indirect Effect on Biogeochemical Cycles and Climate, *Science*,
 994 334, 794-796, doi:10.1126/Science.1207374, 2011.

995 Medlyn, B. E., Duursma, R. A., Eamus, D., Ellsworth, D. S., Prentice, I. C., Barton, C. V.
 996 M., Crous, K. Y., de Angelis, P., Freeman, M., and Wingate, L.: Reconciling the
 997 optimal and empirical approaches to modelling stomatal conductance, *Global Change*
 998 *Biol*, 17, 2134-2144, doi:10.1111/J.1365-2486.2010.02375.X, 2011.

999 Meinshausen, M., Smith, S. J., Calvin, K., Daniel, J. S., Kainuma, M. L. T., Lamarque, J.
 1000 F., Matsumoto, K., Montzka, S. A., Raper, S. C. B., Riahi, K., Thomson, A., Velders,

1001 G. J. M., and van Vuuren, D. P. P.: The RCP greenhouse gas concentrations and their
 1002 extensions from 1765 to 2300, *Climatic Change*, 109, 213-241, doi:10.1007/S10584-
 1003 011-0156-Z, 2011.
 1004 Mercado, L. M., Bellouin, N., Sitch, S., Boucher, O., Huntingford, C., Wild, M., and
 1005 Cox, P. M.: Impact of changes in diffuse radiation on the global land carbon sink,
 1006 *Nature*, 458, 1014-1017, doi:Doi 10.1038/Nature07949, 2009.
 1007 Miller, R. L., Schmidt, G. A., Nazarenko, L. S., Tausnev, N., Bauer, S. E., DelGenio, A.
 1008 D., Kelley, M., Lo, K. K., Ruedy, R., Shindell, D. T., Aleinov, I., Bauer, M., Bleck,
 1009 R., Canuto, V., Chen, Y. H., Cheng, Y., Clune, T. L., Faluvegi, G., Hansen, J. E.,
 1010 Healy, R. J., Kiang, N. Y., Koch, D., Lacis, A. A., LeGrande, A. N., Lerner, J.,
 1011 Menon, S., Oinas, V., Garcia-Pando, C. P., Perlwitz, J. P., Puma, M. J., Rind, D.,
 1012 Romanou, A., Russell, G. L., Sato, M., Sun, S., Tsigaridis, K., Unger, N.,
 1013 Voulgarakis, A., Yao, M. S., and Zhang, J. L.: CMIP5 historical simulations (1850-
 1014 2012) with GISS ModelE2, *J Adv Model Earth Sy*, 6, 441-477,
 1015 doi:10.1002/2013ms000266, 2014.
 1016 Moorcroft, P. R., Hurtt, G. C., and Pacala, S. W.: A method for scaling vegetation
 1017 dynamics: The ecosystem demography model (ED), *Ecol Monogr*, 71, 557-585,
 1018 doi:10.1890/0012-9615(2001)071[0557:Amfsvd]2.0.Co;2, 2001.
 1019 Murray, M. B., Cannell, M. G. R., and Smith, R. I.: Date of Budburst of fifteen Tree
 1020 Species in Britain Following Climatic Warming, *J Appl Ecol*, 26, 693-700,
 1021 doi:10.2307/2404093, 1989.
 1022 O'Keefe, J.: Phenology of Woody Species at Harvard Forest since 1990. Long Term
 1023 Ecological Research Network,
 1024 <http://dx.doi.org/10.6073/pasta/b151c3eb552433a2a94c6f8de489740b>, 2000.
 1025 Oleson, K. W., Lawrence, D. M., Bonan, G. B., Flanne, M. G., Kluzek, E., Lawrence, P.
 1026 J., Levis, S., Swenson, S. C., and Thornton, P. E.: Technical Description of version
 1027 4.0 of the Community Land Model (CLM), National Center for Atmospheric
 1028 Research, Boulder, CONCAR/TN-478+STR, 2010.
 1029 Olson, D. M., Dinerstein, E., Wikramanayake, E. D., Burgess, N. D., Powell, G. V. N.,
 1030 Underwood, E. C., D'amico, J. A., Itoua, I., Strand, H. E., Morrison, J. C., Loucks, C.
 1031 J., Allnutt, T. F., Ricketts, T. H., Kura, Y., Lamoreux, J. F., Wettengel, W. W.,
 1032 Hedao, P., and Kassem, K. R.: Terrestrial Ecoregions of the World: A New Map of
 1033 Life on Earth, *Bioscience*, 51, 933-938, doi:10.1641/0006-
 1034 3568(2001)051[0933:TEOTWA]2.0.CO;2, 2001.
 1035 Pechony, O. and Shindell, D. T.: Fire parameterization on a global scale, *J. Geophys.*
 1036 *Res.*, 114, D16115, doi:10.1029/2009jd011927, 2009.
 1037 Piao, S. L., Sitch, S., Ciais, P., Friedlingstein, P., Peylin, P., Wang, X. H., Ahlstrom, A.,
 1038 Anav, A., Canadell, J. G., Cong, N., Huntingford, C., Jung, M., Levis, S., Levy, P. E.,
 1039 Li, J. S., Lin, X., Lomas, M. R., Lu, M., Luo, Y. Q., Ma, Y. C., Myneni, R. B.,
 1040 Poulter, B., Sun, Z. Z., Wang, T., Viovy, N., Zaehle, S., and Zeng, N.: Evaluation of
 1041 terrestrial carbon cycle models for their response to climate variability and to CO2
 1042 trends, *Global Change Biol*, 19, 2117-2132, doi:10.1111/Gcb.12187, 2013.
 1043 Pieruschka, R., Huber, G., and Berry, J. A.: Control of transpiration by radiation, *P Natl*
 1044 *Acad Sci USA*, 107, 13372-13377, doi:10.1073/Pnas.0913177107, 2010.
 1045 Porporato, A., Laio, F., Ridolfi, L., and Rodriguez-Iturbe, I.: Plants in water-controlled
 1046 ecosystems: active role in hydrologic processes and response to water stress - III.

1047 Vegetation water stress, *Adv Water Resour*, 24, 725-744, doi:10.1016/S0309-
1048 1708(01)00006-9, 2001.

1049 Potter, C. S., Randerson, J. T., Field, C. B., Matson, P. A., Vitousek, P. M., Mooney, H.
1050 A., and Klooster, S. A.: Terrestrial Ecosystem Production - a Process Model-Based
1051 on Global Satellite and Surface Data, *Global Biogeochem Cy*, 7, 811-841,
1052 doi:10.1029/93gb02725, 1993.

1053 Rayner, N. A., Brohan, P., Parker, D. E., Folland, C. K., Kennedy, J. J., Vanicek, M.,
1054 Ansell, T. J., and Tett, S. F. B.: Improved analyses of changes and uncertainties in sea
1055 surface temperature measured in situ since the mid-nineteenth century: The HadSST2
1056 dataset, *J Climate*, 19, 446-469, doi:10.1175/Jcli3637.1, 2006.

1057 Richardson, A. D., Bailey, A. S., Denny, E. G., Martin, C. W., and O'Keefe, J.:
1058 Phenology of a northern hardwood forest canopy, *Global Change Biol*, 12, 1174-
1059 1188, doi:10.1111/j.1365-2486.2006.01164.x, 2006.

1060 Richardson, A. D., Keenan, T. F., Migliavacca, M., Ryu, Y., Sonnentag, O., and Toomey,
1061 M.: Climate change, phenology, and phenological control of vegetation feedbacks to
1062 the climate system, *Agr Forest Meteorol*, 169, 156-173, 2013.

1063 Rienecker, M. M., Suarez, M. J., Gelaro, R., Todling, R., Bacmeister, J., Liu, E.,
1064 Bosilovich, M. G., Schubert, S. D., Takacs, L., Kim, G. K., Bloom, S., Chen, J. Y.,
1065 Collins, D., Conaty, A., Da Silva, A., Gu, W., Joiner, J., Koster, R. D., Lucchesi, R.,
1066 Molod, A., Owens, T., Pawson, S., Pegion, P., Redder, C. R., Reichle, R., Robertson,
1067 F. R., Ruddick, A. G., Sienkiewicz, M., and Woollen, J.: MERRA: NASA's Modern-
1068 Era Retrospective Analysis for Research and Applications, *J Climate*, 24, 3624-3648,
1069 doi:10.1175/Jcli-D-11-00015.1, 2011.

1070 Rosenzweig, C. and Abramopoulos, F.: Land-surface model development for the GISS
1071 GCM, *J Climate*, 10, 2040-2054, doi:10.1175/1520-
1072 0442(1997)010<2040:Lsmdft>2.0.Co;2, 1997.

1073 Sacks, W. J., Deryng, D., Foley, J. A., and Ramankutty, N.: Crop planting dates: an
1074 analysis of global patterns, *Global Ecol Biogeogr*, 19, 607-620, doi:10.1111/J.1466-
1075 8238.2010.00551.X, 2010.

1076 Schaefer, K., Collatz, G. J., Tans, P., Denning, A. S., Baker, I., Berry, J., Prihodko, L.,
1077 Suits, N., and Philpott, A.: Combined Simple Biosphere/Carnegie-Ames-Stanford
1078 Approach terrestrial carbon cycle model, *J. Geophys. Res.*, 113, G03034,
1079 doi:10.1029/2007jg000603, 2008.

1080 Schaefer, K. and co-authors: A model-data comparison of gross primary productivity:
1081 Results from the North American Carbon Program site synthesis, *J. Geophys. Res.*,
1082 117, G03010, doi:10.1029/2012jg001960, 2012.

1083 Schmidt, G. A., Kelley, M., Nazarenko, L., Ruedy, R., Russell, G. L., Aleinov, I., Bauer,
1084 M., Bauer, S. E., Bhat, M. K., Bleck, R., Canuto, V., Chen, Y. H., Cheng, Y., Clune,
1085 T. L., Del Genio, A., de Fainchtein, R., Faluvegi, G., Hansen, J. E., Healy, R. J.,
1086 Kiang, N. Y., Koch, D., Lacis, A. A., LeGrande, A. N., Lerner, J., Lo, K. K.,
1087 Matthews, E. E., Menon, S., Miller, R. L., Oinas, V., Olosio, A. O., Perlwitz, J. P.,
1088 Puma, M. J., Putman, W. M., Rind, D., Romanou, A., Sato, M., Shindell, D. T., Sun,
1089 S., Syed, R. A., Tausnev, N., Tsigaridis, K., Unger, N., Voulgarakis, A., Yao, M. S.,
1090 and Zhang, J. L.: Configuration and assessment of the GISS ModelE2 contributions
1091 to the CMIP5 archive, *J Adv Model Earth Sy*, 6, 141-184,
1092 doi:10.1002/2013ms000265, 2014.

1093 Schmidt, G. A., Ruedy, R., Hansen, J. E., Aleinov, I., Bell, N., Bauer, M., Bauer, S.,
 1094 Cairns, B., Canuto, V., Cheng, Y., Del Genio, A., Faluvegi, G., Friend, A. D., Hall, T.
 1095 M., Hu, Y. Y., Kelley, M., Kiang, N. Y., Koch, D., Lacis, A. A., Lerner, J., Lo, K. K.,
 1096 Miller, R. L., Nazarenko, L., Oinas, V., Perlwitz, J., Perlwitz, J., Rind, D., Romanou,
 1097 A., Russell, G. L., Sato, M., Shindell, D. T., Stone, P. H., Sun, S., Tausnev, N.,
 1098 Thresher, D., and Yao, M. S.: Present-day atmospheric simulations using GISS
 1099 ModelE: Comparison to in situ, satellite, and reanalysis data, *J Climate*, 19, 153-192,
 1100 doi:10.1175/Jcli3612.1, 2006.
 1101 Schuster, C., Estrella, N., and Menzel, A.: Shifting and extension of phenological periods
 1102 with increasing temperature along elevational transects in southern Bavaria, *Plant*
 1103 *Biology*, 16, 332-344, doi:10.1111/Plb.12071, 2014.
 1104 Scott, C. E., Rap, A., Spracklen, D. V., Forster, P. M., Carslaw, K. S., Mann, G. W.,
 1105 Pringle, K. J., Kivekas, N., Kulmala, M., Lihavainen, H., and Tunved, P.: The direct
 1106 and indirect radiative effects of biogenic secondary organic aerosol, *Atmos Chem*
 1107 *Phys*, 14, 447-470, doi:10.5194/Acp-14-447-2014, 2014.
 1108 Shindell, D. T., Lamarque, J. F., Schulz, M., Flanner, M., Jiao, C., Chin, M., Young, P. J.,
 1109 Lee, Y. H., Rotstajn, L., Mahowald, N., Milly, G., Faluvegi, G., Balkanski, Y.,
 1110 Collins, W. J., Conley, A. J., Dalsoren, S., Easter, R., Ghan, S., Horowitz, L., Liu, X.,
 1111 Myhre, G., Nagashima, T., Naik, V., Rumbold, S. T., Skeie, R., Sudo, K., Szopa, S.,
 1112 Takemura, T., Voulgarakis, A., Yoon, J. H., and Lo, F.: Radiative forcing in the
 1113 ACCMIP historical and future climate simulations, *Atmos Chem Phys*, 13, 2939-
 1114 2974, doi:10.5194/Acp-13-2939-2013, 2013a.
 1115 Shindell, D. T., Pechony, O., Voulgarakis, A., Faluvegi, G., Nazarenko, L., Lamarque, J.
 1116 F., Bowman, K., Milly, G., Kovari, B., Ruedy, R., and Schmidt, G. A.: Interactive
 1117 ozone and methane chemistry in GISS-E2 historical and future climate simulations,
 1118 *Atmos Chem Phys*, 13, 2653-2689, doi:10.5194/Acp-13-2653-2013, 2013b.
 1119 Simard, M., Pinto, N., Fisher, J. B., and Baccini, A.: Mapping forest canopy height
 1120 globally with spaceborne lidar, *J. Geophys. Res.*, 116, G04021,
 1121 doi:10.1029/2011jg001708, 2011.
 1122 Sitch, S., Cox, P. M., Collins, W. J., and Huntingford, C.: Indirect radiative forcing of
 1123 climate change through ozone effects on the land-carbon sink, *Nature*, 448, 791-794,
 1124 doi:10.1038/Nature06059, 2007.
 1125 Sitch, S., Friedlingstein, P., Gruber, N., Jones, S. D., Murray-Tortarolo, G., Ahlström, A.,
 1126 Doney, S. C., Graven, H., Heinze, C., Huntingford, C., Levis, S., Levy, P. E., Lomas,
 1127 M., Poulter, B., Viovy, N., Zaehle, S., Zeng, N., Arneth, A., Bonan, G., Bopp, L.,
 1128 Canadell, J. G., Chevallier, F., Ciais, P., Ellis, R., Gloor, M., Peylin, P., Piao, S. L.,
 1129 Quéré, C. L., Smith, B., Zhu, Z., and Myneni, R.: Recent trends and drivers of
 1130 regional sources and sinks of carbon dioxide, *Biogeosciences*, 12, 653-679, 2015.
 1131 Sitch, S., Smith, B., Prentice, I. C., Arneth, A., Bondeau, A., Cramer, W., Kaplan, J. O.,
 1132 Levis, S., Lucht, W., Sykes, M. T., Thonicke, K., and Venevsky, S.: Evaluation of
 1133 ecosystem dynamics, plant geography and terrestrial carbon cycling in the LPJ
 1134 dynamic global vegetation model, *Global Change Biol*, 9, 161-185,
 1135 doi:10.1046/J.1365-2486.2003.00569.X, 2003.
 1136 Spitters, C. J. T., Toussaint, H. A. J. M., and Goudriaan, J.: Separating the Diffuse and
 1137 Direct Component of Global Radiation and Its Implications for Modeling Canopy

1138 Photosynthesis .1. Components of Incoming Radiation, *Agr Forest Meteorol*, 38, 217-
1139 229, doi:10.1016/0168-1923(86)90060-2, 1986.

1140 Stephenson, N. L. and van Mantgem, P. J.: Forest turnover rates follow global and
1141 regional patterns of productivity, *Ecol Lett*, 8, 524-531, doi:10.1111/J.1461-
1142 0248.2005.00746.X, 2005.

1143 Sugiura, D. and Tateno, M.: Optimal Leaf-to-Root Ratio and Leaf Nitrogen Content
1144 Determined by Light and Nitrogen Availabilities, *Plos One*, 6, e22236,
1145 doi:10.1371/journal.pone.0022236, 2011.

1146 Thomas, R. Q., Zaehle, S., Templer, P. H., and Goodale, C. L.: Global patterns of
1147 nitrogen limitation: confronting two global biogeochemical models with observations,
1148 *Global Change Biol*, 19, 2986-2998, doi:10.1111/Gcb.12281, 2013.

1149 Thornton, P. E., Lamarque, J. F., Rosenbloom, N. A., and Mahowald, N. M.: Influence of
1150 carbon-nitrogen cycle coupling on land model response to CO₂ fertilization and
1151 climate variability, *Global Biogeochem Cy*, 21, Gb4018, doi:10.1029/2006gb002868,
1152 2007.

1153 Unger, N.: Global climate impact of civil aviation for standard and desulfurized jet fuel,
1154 *Geophys. Res. Lett.*, 38, L20803, doi:10.1029/2011gl049289, 2011.

1155 Unger, N.: Human land-use-driven reduction of forest volatiles cools global climate, *Nat*
1156 *Clim Change*, 4, 907-910, doi:10.1038/Nclimate2347, 2014a.

1157 Unger, N.: Isoprene emission variability through the twentieth century, *J. Geophys. Res.*,
1158 118, 13606-13613, doi:10.1002/2013jd020978, 2013.

1159 Unger, N.: On the role of plant volatiles in anthropogenic global climate change,
1160 *Geophys Res Lett*, 41, 8563-8569, doi:10.1002/2014gl061616, 2014b.

1161 Unger, N., Harper, K., Zheng, Y., Kiang, N. Y., Aleinov, I., Arneth, A., Schurgers, G.,
1162 Amelynck, C., Goldstein, A., Guenther, A., Heinesch, B., Hewitt, C. N., Karl, T.,
1163 Laffineur, Q., Langford, B., McKinney, K. A., Misztal, P., Potosnak, M., Rinne, J.,
1164 Pressley, S., Schoon, N., and Serça, D.: Photosynthesis-dependent isoprene emission
1165 from leaf to planet in a global carbon–chemistry–climate model, *Atmos. Chem. Phys.*,
1166 13, 17717-17791, doi:10.5194/acp-13-10243-2013, 2013.

1167 Unger, N. and Yue, X.: Strong chemistry- climate feedbacks in the Pliocene, *Geophys.*
1168 *Res. Lett.*, 41, 527-533, doi:10.1002/2013gl058773, 2014.

1169 Val Martin, M., Heald, C. L., and Arnold, S. R.: Coupling dry deposition to vegetation
1170 phenology in the Community Earth System Model: Implications 3 for the simulation
1171 of surface O₃, *Geophys. Res. Lett.*, 8, 2988-2996, doi:10.1002/2014GL059651, 2014.

1172 Vitasse, Y., Delzon, S., Dufrene, E., Pontailier, J. Y., Louvet, J. M., Kremer, A., and
1173 Michalet, R.: Leaf phenology sensitivity to temperature in European trees: Do within-
1174 species populations exhibit similar responses?, *Agr Forest Meteorol*, 149, 735-744,
1175 doi:10.1016/J.Agrformet.2008.10.019, 2009.

1176 von Caemmerer, S. and Farquhar, G. D.: Some Relationships between the Biochemistry
1177 of Photosynthesis and the Gas-Exchange of Leaves, *Planta*, 153, 376-387, 1981.

1178 Weedon, G. P., Balsamo, G., Bellouin, N., Gomes, S., Best, M. J., and Viterbo, P.: The
1179 WFDEI meteorological forcing data set: WATCH Forcing Data methodology applied
1180 to ERA-Interim reanalysis data, *Water Resources Research*, 50, 7505-7514,
1181 doi:10.1002/2014wr015638, 2014.

- White, M. A., Thornton, P. E., and Running, S. W.: A continental phenology model for monitoring vegetation responses to interannual climatic variability, *Global Biogeochem Cy*, 11, 217-234, doi:10.1029/97gb00330, 1997.
- Wittig, V. E., Ainsworth, E. A., and Long, S. P.: To what extent do current and projected increases in surface ozone affect photosynthesis and stomatal conductance of trees? A meta-analytic review of the last 3 decades of experiments, *Plant Cell Environ*, 30, 1150-1162, doi:10.1111/J.1365-3040.2007.01717.X, 2007.
- Yienger, J. J. and Levy, H.: Empirical-Model of Global Soil-Biogenic Nox Emissions, *J. Geophys. Res.*, 100, 11447-11464, doi:10.1029/95jd00370, 1995.
- Yue, X. and Unger, N.: Ozone vegetation damage effects on gross primary productivity in the United States, *Atmos. Chem. Phys.*, 14, 9137-9153, doi:10.5194/acp-14-9137-2014, 2014.
- Yue, X., Unger, N., Keenan, T. F., Zhang, X., and Vogel, C. S.: Probing the past 30-year phenology trend of U.S. deciduous forests, *Biogeosciences Discuss.*, 12, 6037-6080, doi:10.5194/bgd-12-6037-2015, 2015a.
- Yue, X., Unger, N., and Zheng, Y.: Distinguishing the drivers of trends in land carbon fluxes and biogenic emissions over the past three decades, *Atmos. Chem. Phys.*, submitted, 2015b.
- Zaehle, S., Medlyn, B. E., De Kauwe, M. G., Walker, A. P., Dietze, M. C., Hickler, T., Luo, Y. Q., Wang, Y. P., El-Masri, B., Thornton, P., Jain, A., Wang, S. S., Warlind, D., Weng, E. S., Parton, W., Iversen, C. M., Gallet-Budynnek, A., McCarthy, H., Finzi, A. C., Hanson, P. J., Prentice, I. C., Oren, R., and Norby, R. J.: Evaluation of 11 terrestrial carbon-nitrogen cycle models against observations from two temperate Free-Air CO₂ Enrichment studies, *New Phytol*, 202, 803-822, doi:10.1111/Nph.12697, 2014.
- Zeng, N., Mariotti, A., and Wetzal, P.: Terrestrial mechanisms of interannual CO₂ variability, *Global Biogeochem Cy*, 19, Gb1016, doi:10.1029/2004gb0022763, 2005.
- Zhang, X. Y., Tan, B., and Yu, Y. Y.: Interannual variations and trends in global land surface phenology derived from enhanced vegetation index during 1982-2010, *Int J Biometeorol*, 58, 547-564, doi:10.1007/S00484-014-0802-Z, 2014.
- Zhao, M. S., Heinsch, F. A., Nemani, R. R., and Running, S. W.: Improvements of the MODIS terrestrial gross and net primary production global data set, *Remote Sens Environ*, 95, 164-176, doi:10.1016/J.Rse.2004.12.011, 2005.
- Zhao, M. S. and Running, S. W.: Drought-Induced Reduction in Global Terrestrial Net Primary Production from 2000 Through 2009, *Science*, 329, 940-943, doi:10.1126/Science.1192666, 2010.
- Zheng, Y., Unger, N., Barley, M., and Yue, X.: Relationships between photosynthesis and formaldehyde as a probe of isoprene emission, *Atmos. Chem. Phys. Discuss.*, 15, 11763-11797, doi:10.5194/acpd-15-11763-2015, 2015.
- Zhu, Z. C., Bi, J., Pan, Y. Z., Ganguly, S., Anav, A., Xu, L., Samanta, A., Piao, S. L., Nemani, R. R., and Myneni, R. B.: Global Data Sets of Vegetation Leaf Area Index (LAI)_{3g} and Fraction of Photosynthetically Active Radiation (FPAR)_{3g} Derived from Global Inventory Modeling and Mapping Studies (GIMMS) Normalized Difference Vegetation Index (NDVI_{3g}) for the Period 1981 to 2011, *Remote Sens*, 5, 927-948, doi:10.3390/Rs5020927, 2013.

1228 **Table 1.** Photosynthetic and allometric parameters for the vegetation model.
1229

PFT ^a	TDA	GRAC3	GRAC4	SHR	DBF	ENF	EBF	CROC3	CROC4
Carboxylation	C3	C3	C4	C3	C3	C3	C3	C3	C4
V_{cmax25} ($\mu\text{mol m}^{-2} \text{s}^{-1}$)	33	43	24	38	45	43	40	40	40
m	9	9	5	9	9	9	9	11	5
b ($\text{mmol m}^{-2} \text{s}^{-1}$)	2	2	2	2	2	2	2	8	2
a_{wl} (kg C m^{-2})	0.1	0.005	0.005	0.1	0.95	0.85	0.95	0.005	0.005
b_{wl}	1.667	1.667	1.667	1.667	1.667	1.667	1.667	1.667	1.667
σ_l (kg C m^{-2} LAI^{-1})	0.05	0.025	0.05	0.05	0.0375	0.1	0.0375	0.025	0.05
η (kg C m^{-1} LAI^{-1})	0.01	0.01	0.01	0.01	0.01	0.01	0.01	0.01	0.01
n_0 ($\text{kg N} [\text{kg C}]^{-1}$)	0.06	0.073	0.06	0.06	0.046	0.033	0.046	0.073	0.06
n_{rl}	0.5	1	1	0.5	0.5	0.75	0.5	1	1
n_{wl}	0.1	1	1	0.1	0.1	0.1	0.1	1	1
r_g	0.2	0.2	0.2	0.2	0.2	0.2	0.2	0.2	0.2
LAI_{min}	1	1	1	1	1	1	1	1	1
LAI_{max}	3	3	3	3	9	5	9	3	3
γ_r (360 days) ⁻¹	0.5	0.75	0.75	0.5	0.75	0.25	0.75	0.75	0.75
γ_w (360 days) ⁻¹	0.1	0.2	0.2	0.1	0.015	0.01	0.015	0.2	0.2
H_0 (m)	1	0.8	1.3	1	19	16.5	19	0.8	1.3

1230
1231 ^a Plant functional types (PFTs) are tundra (TDA), C3 grassland (GRAC3), C4
1232 savanna/grassland (GRAC4), shrubland (SHR), deciduous broadleaf forest (DBF),
1233 evergreen needleleaf forest (ENF), evergreen broadleaf forest (EBF), and C3/C4 cropland
1234 (CROC3/CROC4).
1235

1236
1237
1238
1239

Table 2. Phenological parameters for the vegetation model.

Variables	Description	Units	Value	Reference
T_b	Base temperature for budburst forcing	°C	5	Murray et al. (1989)
a	Parameters for budburst threshold G_b	Degree day	-110	Calibrated (Y2015)
b	Parameters for budburst threshold G_b	Degree day	550	Calibrated (Y2015)
r	Parameters for budburst threshold G_b	Dimensionless	-0.01	Murray et al. (1989)
L_g	Growing length	Degree day	380	Calibrated (Y2015)
T_s	Base temperature for senescence forcing	°C	20	Dufrene et al. (2005)
F_s	Threshold for leaf fall	Degree day	-140	Calibrated (Y2015)
L_f	Falling length	Degree day	410	Calibrated (Y2015)
P_x	Daylength threshold for leaf fall	Minutes	695	White et al. (1997)
P_i	Daylength threshold for full dormancy	Minutes	585	Calibrated (Y2015)
T_d	Threshold for drought phenology	°C	12	Calibrated (Fig. 2)
β_{\min}	Lower threshold of drought limit for shrub	Dimensionless	0.4	Calibrated (Fig. S1)
β_{\max}	Upper threshold of drought limit for shrub	Dimensionless	1	Calibrated (Fig. S1)
ST_b	Base soil temperature for budburst forcing	°C	0	White et al. (1997)
SG_b	Threshold for budburst with soil temperature	Degree day	100	Calibrated
SL_g	Growing length with soil temperature	Degree day	100	Calibrated
ST_s	Base soil temperature for senescence forcing	°C	10	Calibrated
SF_s	Threshold for leaf fall with soil temperature	Degree day	-80	Calibrated
SL_f	Falling length with soil temperature	Degree day	100	Calibrated
β_{\min}	Lower threshold of drought limit for herbs	Dimensionless	0.3	Calibrated (Fig. S1)
β_{\max}	Upper threshold of drought limit for herbs	Dimensionless	0.9	Calibrated (Fig. S1)

1240
1241
1242

1243
1244
1245
1246
1247
1248
1249

Table 3. Summary of carbon fluxes and ozone vegetation damage in different domains and for tropics (23°S-23°N).

Regions	Amazon	North America	Central Africa	Europe	East Asia	Indonesia	Tropics	Global
GPP (Pg C a ⁻¹)	33.4	12.3	25.7	11.5	17.9	6.7	77.9	124.6
NPP (Pg C a ⁻¹)	15.5	7.5	12.1	7.3	10.3	2.9	36.8	65
NEE (Pg C a ⁻¹)	-0.4	-0.5	-0.3	-0.4	-0.5	-0.1	-1.0	-2.5
Ra (Pg C a ⁻¹)	17.9	4.8	13.6	4.2	7.6	3.8	41.1	59.6
Rh (Pg C a ⁻¹)	15.1	7	11.8	6.9	9.8	2.8	35.8	62.5
Low ozone damage to GPP (%)	-0.9	-2.4	-1.8	-2.5	-4.3	-3	-1.7	-2.1
High ozone damage to GPP (%)	-2.6	-5.8	-4.4	-6.1	-9.6	-7.3	-4.4	-5
Low ozone damage to LAI (%)	-0.3	-0.5	-0.6	-0.5	-0.9	-0.8	-0.5	-0.5
High ozone damage to LAI (%)	-0.8	-1.2	-1.6	-1.4	-2.4	-2.1	-1.4	-1.4

1250
1251
1252
1253
1254

Figure captions

Figure 1. Distribution of 145 sites from the FLUXNET and the North American Carbon Program (NACP) network. The duplicated sites have been removed. The color indicates different plant functional types (PFTs) as evergreen needleleaf forest (ENF, blue), evergreen broadleaf forest (EBF, cyan), deciduous broadleaf forest (DBF, magenta), shrubland (SHR, yellow) grassland (GRA, green), and cropland (CRO, red). “Mixed Forests” are classified as ENF, “Permanent Wetlands”, “Savannas”, and “Woody Savannas” as SHR. The PFT of each site is described in supplemental Table S1.

Figure 2. Correlations between monthly gross primary productivity (GPP) and soil variables at (a, b) shrub and (c, d) grass sites. For each site, we calculate correlation coefficients of GPP-soil temperature (red points) and GPP-soil moisture (blue squares). These correlation coefficients are then plotted against the annual mean (a, c) soil temperature ($^{\circ}\text{C}$) or (b, d) soil moisture (fraction) at each site.

Figure 3. Comparison between observed and simulated monthly GPP from FLUXNET and NACP networks grouped by PFTs. Each point represents the average value of one month at one site. The red lines indicate linear regression between observations and simulations. The regression fit, correlation coefficient, and relative bias are shown on each panel. The PFTs include evergreen needleleaf forest (ENF), evergreen broadleaf forest (EBF), deciduous broadleaf forest (DBF), shrubland (SHR), grassland (GRA), and cropland (CRO). The detailed comparison for each site is shown in Fig. S2. Units of GPP: $\text{g C m}^{-2} \text{ day}^{-1}$.

Figure 4. Bar charts of (a, d) correlation coefficients (R), (b, e) biases, and (c, f) RMSE for monthly (a, b, c) GPP and (d, e, f) net ecosystem exchange (NEE) between simulations and observations at 145 sites. Each bar represents the number of sites where the R , bias, or RMSE of simulations fall between the specific ranges as defined by the x-axis intervals. The minimum and maximum of each statistical metric are indicated as the two ends of x-axis in the plots. The values of x-axis are not even. The absolute biases

instead of relative biases are shown for NEE because the long-term average NEE (the denominator) is usually close to zero at most sites. The PFT definitions are: ENF, Evergreen Needleleaf Forest; EBF, Evergreen Broadleaf Forest; DBF, Deciduous Broadleaf Forest; SHR, Shrubland; GRA, Grasslands; CRO, Croplands. Detailed comparisons at each site are shown in Figs. S2 and S4.

Figure 5. Simulated (a) tree height, (c) leaf area index (LAI), and (e) GPP and their differences relative to observations (b, d, f). GPP dataset is from Jung et al. (2009). Simulations are performed with WFDEI reanalysis. Statistics are the annual average for period 1982-2011. The boxes in (a) represent six regions used for seasonal comparison in Fig. 6.

Figure 6. Comparison of annual (a) tree height and seasonal (b) LAI, (c) GPP, and (d) net primary productivity (NPP) between simulations and observations for the six regions shown in Fig. 5a. GPP dataset is from Jung et al. (2009). Values at different regions are marked using different symbols, with distinct colors indicating seasonal means for winter (blue, December-February), spring (green, March-May), summer (red, June-August), and autumn (magenta, September-November).

Figure 7. Comparison of simulated global GPP and net biome productivity (NBP) from (red) YIBs-offline and (blue) ModelE2-YIBs models with 10 other carbon cycle models for 1982-2008. Each black symbol represents an independent model as summarized in Piao et al. (2013). Error bars indicate the standard deviations for interannual variability. The gray shading represents global residual land sink (RLS) calculated in Friedlingstein et al. (2010). The green line on the top represents range of GPP for 1982-2008 estimated by Jung et al. (2011) and the magenta line represents GPP for 1982-2011 from Jung et al. (2009).

Figure 8. Comparison of simulated budburst dates in Northern Hemisphere with remote sensing. Simulated phenology in each grid square is the composite result from DBF, tundra, shrubland, and grassland based on PFT fraction and LAI in that grid box. Both

1317 simulations and observations are averaged for period 1982-2011. Results for Southern
1318 Hemisphere are not shown due to the limit coverage of deciduous forests and cold grass
1319 species.

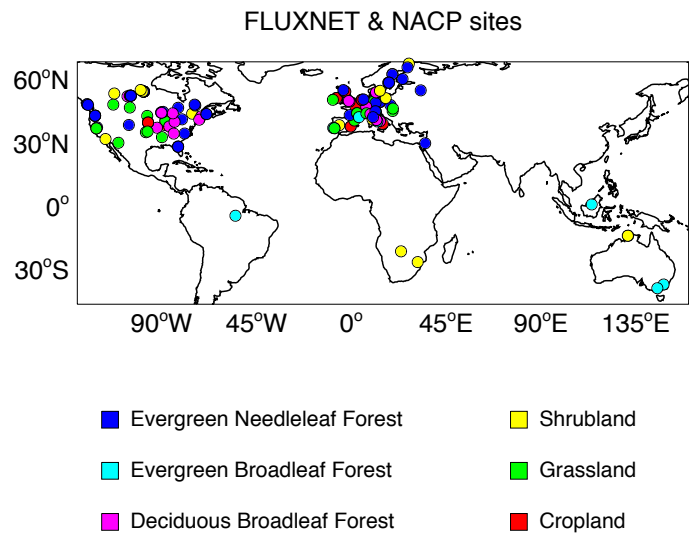
1320

1321 **Figure 9.** Percentage of ozone vegetation damage to (top) GPP and (bottom) LAI with (a,
1322 c) low and (b, d) high sensitivity. Both damages of GPP and LAI are averaged for 1982-
1323 2011. Offline surface ozone concentrations (Fig. S5) are simulated by GISS ModelE2
1324 with climatology of the year 2000.

1325

1326

1327
1328
1329



1330 **Figure 1.** Distribution of 145 sites from the FLUXNET and the North American Carbon
1331 Program (NACP) network. The duplicated sites have been removed. The color indicates
1332 different plant functional types (PFTs) as evergreen needleleaf forest (ENF, blue),
1333 evergreen broadleaf forest (EBF, cyan), deciduous broadleaf forest (DBF, magenta),
1334 shrublands (SHR, yellow) grasslands (GRA, green), and croplands (CRO, red). “Mixed
1335 Forests” are classified as ENF, “Permanent Wetlands”, “Savannas”, and “Woody
1336 Savannas” as SHR. The PFT of each site is described in supplemental Table S1.
1337
1338

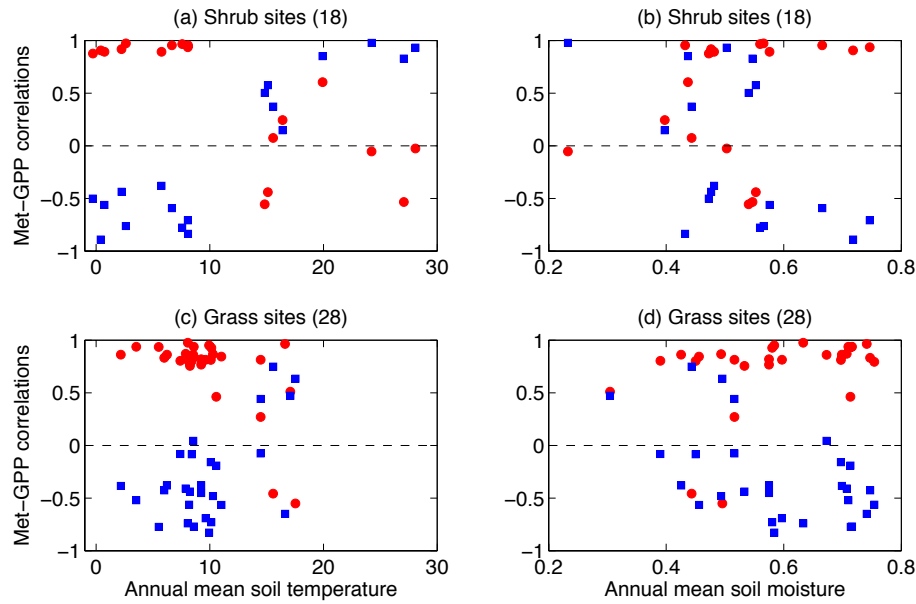


Figure 2. Correlations between monthly gross primary productivity (GPP) and soil variables at (a, b) shrub and (c, d) grass sites. For each site, we calculate correlation coefficients of GPP-soil temperature (red points) and GPP-soil moisture (blue squares). These correlation coefficients are then plotted against the annual mean (a, c) soil temperature ($^{\circ}\text{C}$) or (b, d) soil moisture (fraction) at each site.

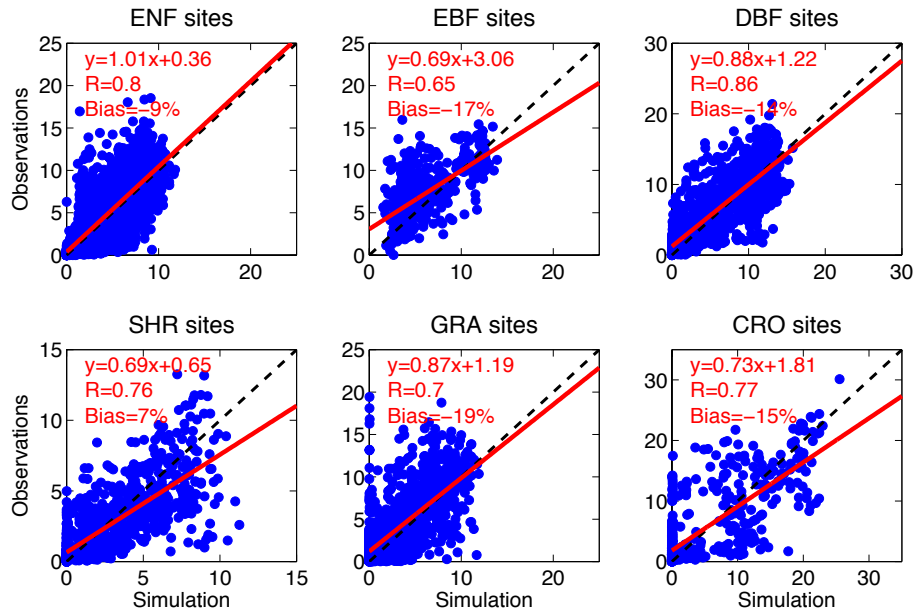
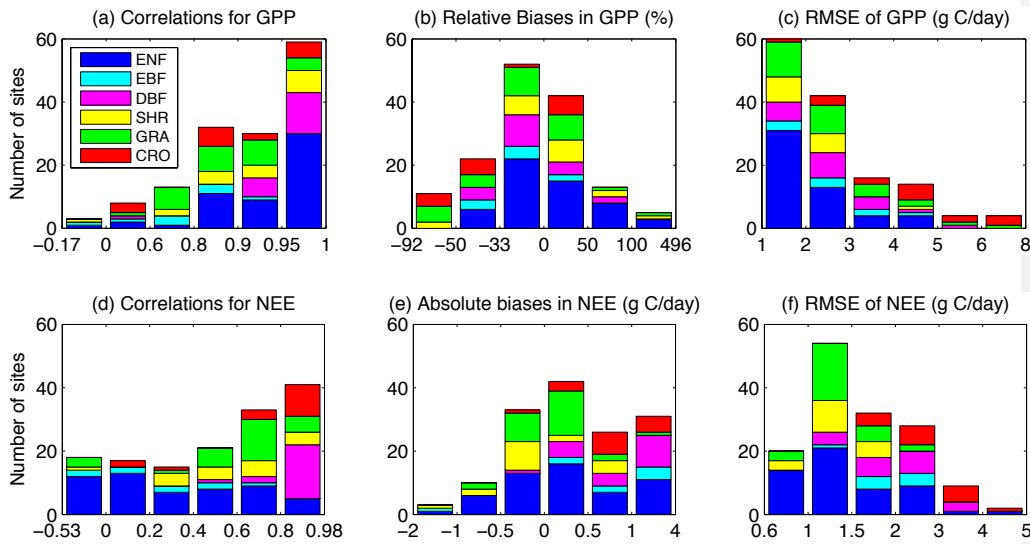


Figure 3. Comparison between observed and simulated monthly GPP from FLUXNET and NACP networks grouped by PFTs. Each point represents the average value of one month at one site. The red lines indicate linear regression between observations and simulations. The regression fit, correlation coefficient, and relative bias are shown on each panel. The PFTs include evergreen needleleaf forest (ENF), evergreen broadleaf forest (EBF), deciduous broadleaf forest (DBF), shrublands (SHR), grasslands (GRA), and croplands (CRO). The detailed comparison for each site is shown in Fig. S2. Units of GPP: $\text{g C m}^{-2} \text{ day}^{-1}$.

1372
1373



1374

1375

1376

1377

1378

1379

1380

1381

1382

1383

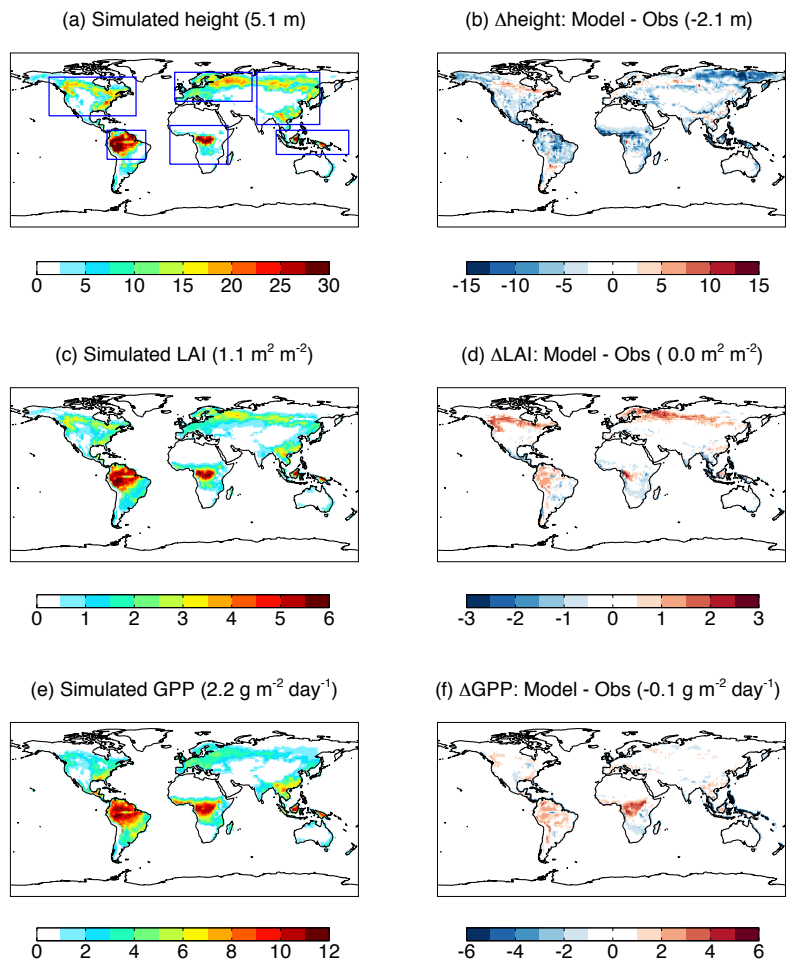
1384

1385

1386

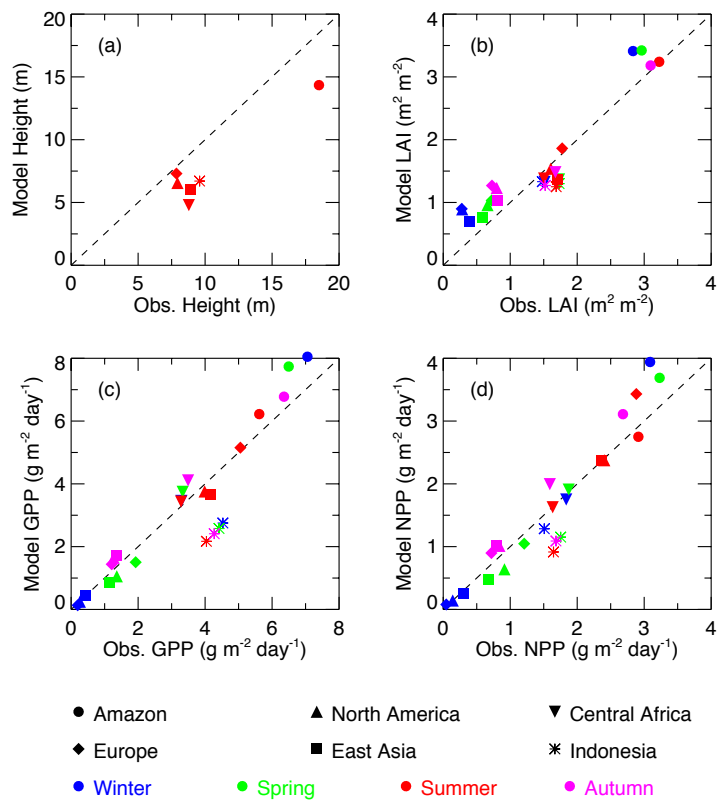
1387

Figure 4. Bar charts of (a, d) correlation coefficients (R), (b, e) biases, and (c, f) RMSE for monthly (a, b, c) GPP and (d, e, f) net ecosystem exchange (NEE) between simulations and observations at 145 sites. Each bar represents the number of sites where the R , bias, or RMSE of simulations fall between the specific ranges as defined by the x-axis intervals. The minimum and maximum of each statistical metric are indicated as the two ends of x-axis in the plots. The values of x-axis are not even. The absolute biases instead of relative biases are shown for NEE because the long-term average NEE (the denominator) is usually close to zero at most sites. The PFT definitions are: ENF, Evergreen Needleleaf Forest; EBF, Evergreen Broadleaf Forest; DBF, Deciduous Broadleaf Forest; SHR, Shrubland; GRA, Grasslands; CRO, Croplands. Detailed comparisons at each site are shown in Figs. S2 and S4.



1389 **Figure 5.** Simulated (a) tree height, (c) leaf area index (LAI), and (e) GPP and their
1390 differences relative to observations (b, d, f). GPP dataset is from Jung et al. (2009).
1391 Simulations are performed with WFDEI reanalysis. Statistics are the annual average for
1392 period 1982-2011. The boxes in (a) represent six regions used for seasonal comparison in
1393 Fig. 6.
1394
1395

1396
1397



1398
1399
1400
1401
1402
1403
1404
1405
1406
1407

Figure 6. Comparison of annual (a) tree height and seasonal (b) LAI, (c) GPP, and (d) net primary productivity (NPP) between simulations and observations for the six regions shown in Fig. 5a. GPP dataset is from Jung et al. (2009). Values at different regions are marked using different symbols, with distinct colors indicating seasonal means for winter (blue, December-February), spring (green, March-May), summer (red, June-August), and autumn (magenta, September-November).

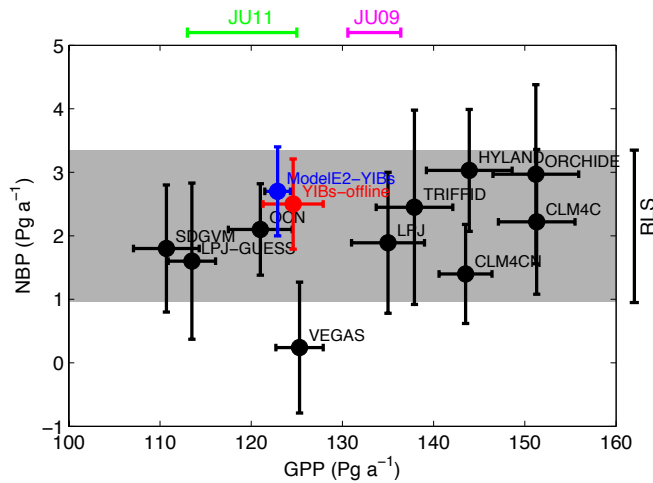


Figure 7. Comparison of simulated global GPP and net biome productivity (NBP) from (red) YIBs-offline and (blue) ModelE2-YIBs models with 10 other carbon cycle models for 1982-2008. Each black symbol represents an independent model as summarized in Piao et al. (2013). Error bars indicate the standard deviations for interannual variability. The gray shading represents global residual land sink (RLS) calculated in Friedlingstein et al. (2010). The green line on the top represents range of GPP for 1982-2008 estimated by Jung et al. (2011) and the magenta line represents GPP for 1982-2011 from Jung et al. (2009).

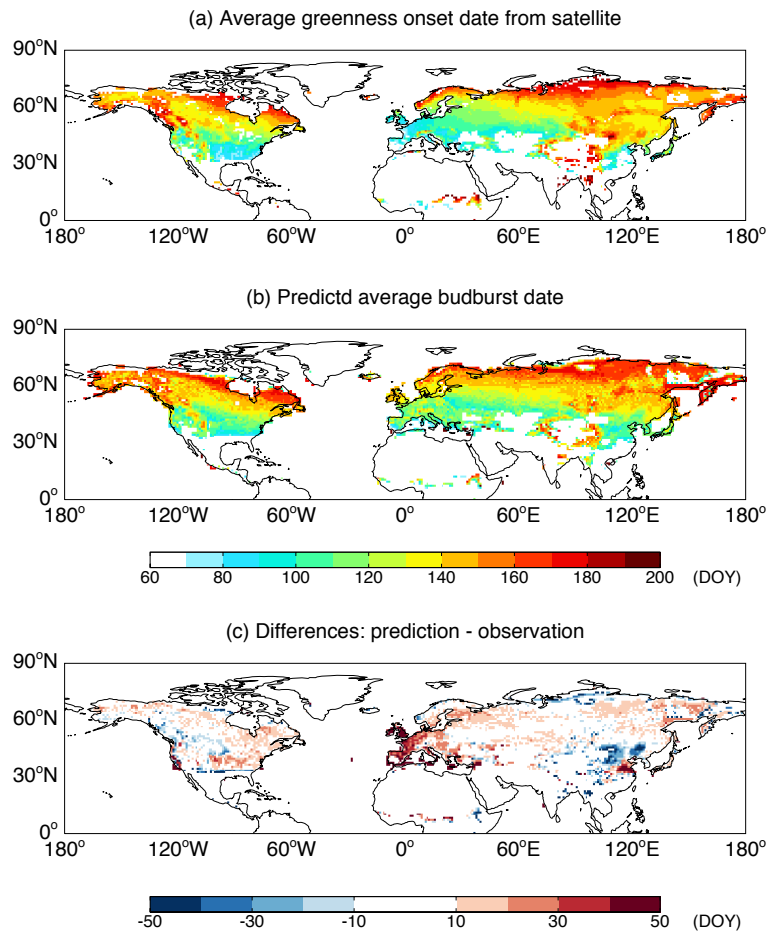
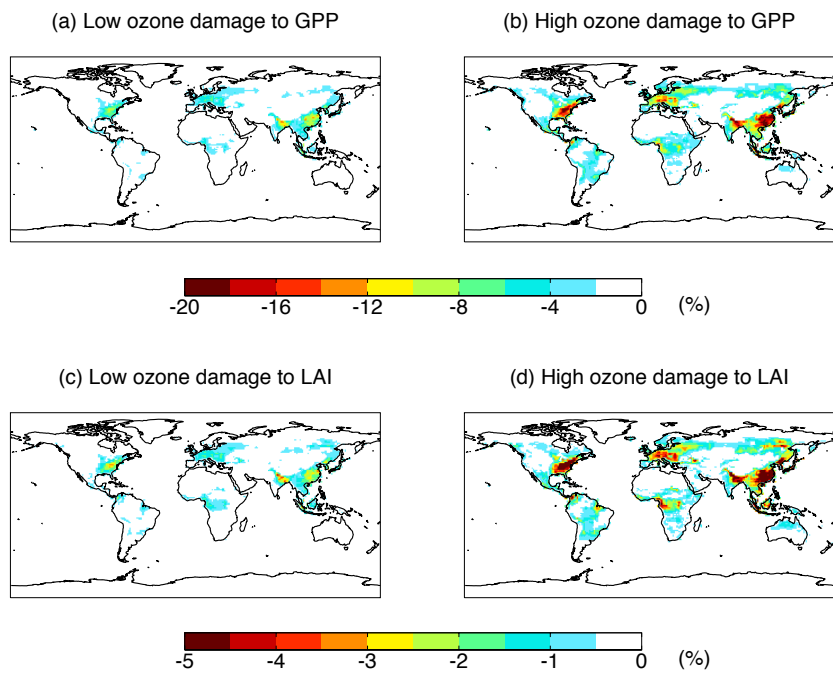


Figure 8. Comparison of simulated budburst dates in Northern Hemisphere with remote sensing. Simulated phenology in each grid square is the composite result from DBF, tundra, shrubland, and grassland based on PFT fraction and LAI in that grid box. Both simulations and observations are averaged for period 1982-2011. Results for Southern Hemisphere are not shown due to the limit coverage of deciduous forests and cold grass species.

1453
1454
1455
1456



1457
1458
1459
1460
1461
1462
1463
1464
1465
1466
1467
1468
1469
1470
1471

Figure 9. Percentage of ozone vegetation damage to (top) GPP and (bottom) LAI with (a, c) low and (b, d) high sensitivity. Both damages of GPP and LAI are averaged for 1982-2011. Offline surface ozone concentrations (Fig. S5) are simulated by GISS ModelE2 with climatology of the year 2000.